1 **Microphysical modelling of aerosol scavenging by different types of clouds.**

2 **Description and validation of the approach**

4 Pascal Lemaitre[1], Arnaud Quérel[2], Alexis Dépée[1], Alice Guerra Devigne[1], Marie Monier[3,4], Thibault Hiron[3], Chloé Soto Minguez[1], Daniel Hardy[5], Andrea
5 Flossmann[3,4]

7 [1] { Institut de Radioprotection et de Sûreté Nucléaire (IRSN), PSN-RES/SCA/LPMA, F-91400, Saclay, France}

8 [2] { Institut de Radioprotection et de Sûreté Nucléaire (IRSN), PSE-SANTE/SESUC/BMCA, F-92260, Fontenay-aux-Roses, France}

9 [3] {Clermont University, Blaise Pascal University, Physical Meteorology Laboratory, Clermont-Ferrand, France}

10 [4] {CNRS, INSU, UMR 6016, LaMP, Aubière, France}

11 [5] {School of Chemistry, University of Bristol, Bristol, BS8 1TS, United Kingdom.

12 Correspondence to: P. Lemaitre (pascal.lemaitre@irsn.fr & arnaud.querel@irsn.fr )

## Short abstract

15 A new in-cloud scavenging scheme is proposed. It is based on a microphysical model of cloud formation and may be applied to long-distance atmospheric

16 transport models (>100 km) and climatic models. This model is applied to for the two most extreme precipitating cloud types, in terms of both relative

17 humidity and vertical extension: cumulonimbus and stratus.

## Abstract

20 With dry deposition and below-cloud scavenging, in-cloud scavenging is one of the three components of aerosol transfer from the atmosphere to the ground.

21 There is no experimental validation of in-cloud particle scavenging models for all cloud types that is not impacted by uncertainties concerning below-cloud

22 scavenging. In this article, the choice was made to start with a recognised and validated microphysical cloud formation model (DESCAM) to extract a scheme

23 of aerosol scavenging by clouds, valid for different cloud types. The resulting model works for the two most extreme precipitation clouds: from

24 cumulonimbus to stratus. It is based on data accessible a priori from Numerical Weather Prediction (NWP) outputs, i.e., the intensity of the rain and the

25 relative humidity in the cloud. The diagnostic of the altitude of the cloud base proves to be a key parameter, and accuracy in this regard is vital. This new in-

26 cloud scavenging scheme is intended for use in long-distance (> 100 km) Atmospheric Transport Models (ATMs) or Global Climate Models (GCMs).

27

## Introduction

29

30 Clouds are an essential component of the troposphere. They play a central role in meteorological forecasting and in the water cycle on the planet (Zhang *et*

31 *al.*, 2020). Similarly, by interacting with solar radiation, they make a significant contribution to the terrestrial radiation balance (Twomey, 1974; Wang and

32 Su, 2013). Moreover, they are often cited as one of the main sources of uncertainty in climate prediction models (Bony and Dufresne, 2005; Palmer, 2014).

33 They can seriously disrupt air traffic, and even produce aircraft crashes (e. g. Air France flight 447 Rio-Paris air disaster).

34 By scavenging aerosols, they contribute to improve air quality (Leaitch *et al.*, 1987; Sievering *et al.*,1984), but also to impact soil pollution, through the

35 deposition of atmospheric pollutants via precipitation (Clark and Smith, 1988; Flossmann, 1998). In case of severe nuclear accidents, radioactive aerosol

36 particles might be released into the troposphere (De Cort, 1998 ; Baklanov and Sørensen, 2001 ; Adachi *et al.*, 2013). When radionuclides are emitted into

37 the environment, it is essential, in order to protect populations, to jointly assess the concentrations of radioactive aerosols in the atmospheric boundary

38 layer, as well as their transfer to the ground. Thus, while an accident is occurring, it is necessary to accurately assess the exposures of populations, both by

39 inhalation and by ingestion (Mathieu *et al.,* 2004; Quélo *et al.,* 2007; Quérel *et al.,* 2012).

40 In nature, deposition of aerosols (and therefore a fortiori of particulate radionuclides) on the ground consists of the contribution of dry deposition and of

41 wet deposition (Slinn 1977). Dry deposition is approximately 1000 times less effective than wet deposition but is the only mechanism operating when there

42 is no precipitation. To date, there are still many uncertainties about the modelling of these two deposition pathways (Petroff *et al.,* 2008, Croft *et al.,* 2010

43 and Ervens, 2015).

44  Flossmann (1998) used the DESCAM model (Flossmann *et al.,* 1985, 1987, 1988) to assess that, for a droplet from a convective cloud, about 70% of the mass

45  of particles the droplet contains when deposited on the ground was incorporated into the droplet in the cloud. This result is consistent with the

46  measurements in the environment of Laguionie *et al.,* (2014), which estimate the cloud to be 60% responsible for the total downwash of particles.

47  Our objective in this article is to establish theoretically a scavenging coefficient applicable to clouds. Scavenging by clouds is more challenging to model than

48  scavenging by rain, under the cloud, as it is much more sensitive to certain input parameters. Rain scavenging is only controlled by a single microphysical

49  mechanism: collection by raindrops (Kerker and Hampl, 1974; Beard, 1974; Grover *et al.,* 1977; Wang and Pruppacher, 1977; Lai *et al.,* 1978; Pranesha and

50  Kamra, 1996; Vohl *et al.,* 1999; Quérel *et al.,* 2014; Lemaitre *et al.,* 2017), whereas cloud scavenging encompasses a set of mechanisms which will firstly

51  make it possible to incorporate aerosols into the cloud droplets (activation, collection, ice nucleation, collection by crystals) then, secondly, to convert a

52  fraction of the cloud hydrometeors into raindrops (condensation, coalescence, Bergeron effects). Only after raindrops have been deposited on the ground

53  is the atmosphere washed out and, by the same process, the soil contaminated. Furthermore, most atmospheric transport models use significantly different

54  schemes to model scavenging by cloud and by rain. Quérel *et al.,* 2021 summarised a few of them in Table 3 of their article.

55  Therefore, in theoretically assessing cloud scavenging, the use of a cloud formation model such as DESCAM (DEtailed SCAvenging Model), forms a good

56  foundation. This model, developed by Andrea Flossmann and her group since the mid-80s (Flossmann *et al.,* 1985; Flossmann, 1998; Monier *et al.,* 2006;

57  Leroy *et al.,* 2007; Planche *et al.,* 2007; Flossmann and Wobrock, 2010; Hiron and Flossmann, 2015; Dépée, 2019), makes it possible, through a detailed

58  microphysical description, to model clouds from their formation through to precipitation, and to monitor the aerosols and what becomes of them once

59  incorporated into the droplets.

60  In this article, we will show how, using a model like DESCAM, it is possible to theoretically calculate a scavenging coefficient in the cloud, on the scale of the

61  cloud system. We will apply this approach to two extreme types of cloud: a cumulonimbus (CCOPE, Dye *et al.,* 1986) and a stratus (Zhang *et al.,* 2004). This

62  approach will then be compared to the models derived from the deposits observed following the Fukushima nuclear accident (Leadbetter *et al.,* 2015; Quérel

63  *et al.,* 2021). Finally, in the last part we will present, a theoretical scheme of the scavenging coefficient, applicable to any type of cloud, will be proposed.

64  We begin by considering some key elements of the theoretical context and some definitions.

## 1. Definitions and theoretical context

### 1.1. Definition of cloud scavenging

67  In large range transport models, the description of scavenging shall remain simple, the operational scientific community models it through a parametrisation

68  involving the cloud scavenging coefficient ($\Lambda_{cloud}$). It is defined as the fraction of pollutants that is transferred from the atmosphere to precipitation (then

69  to the ground) per unit of time. In this article, we will focus on pollutants carried by aerosols (and not gaseous pollutants). The scavenging coefficient is

70  therefore defined spectrally thus:

71
$$\left.\frac{d\mathcal{N}(d_{ap})}{\mathcal{N}(d_{ap})}\right|_{cloud} = \left.\frac{d\mathcal{M}(d_{ap})}{\mathcal{M}(d_{ap})}\right|_{cloud} = -\Lambda_{cloud}(d_{ap}).dt \qquad \text{Equation 1}$$

72  In this equation $\mathcal{N}(d_{ap})$ and $\mathcal{M}(d_{ap})$ are respectively the concentrations in number and in mass of aerosols of diameter $d_{ap}$ per unit of air volume;

73  likewise, $d\mathcal{N}(d_{ap})$ and $d\mathcal{M}(d_{ap})$ are respectively the variations in concentration in number and in mass of aerosols of diameter $d_{ap}$, in relation to their

74  transfer into precipitation, per unit of time. The two definitions are considered equal when expressed spectrally, assuming a uniform density of all aerosol

75  particles. In this study, we specifically considered aerosol particles composed of ammonium sulphate, thus confirming this equality. However, in real

76  atmospheric conditions, aerosol particle density is typically not uniform. In such cases, it becomes crucial to specify whether we are referring to a mass

77  scavenging coefficient or a number one. To prevent any confusion, in the rest of the article, the exponent $m$ is introduced to the scavenging coefficient

78  $\Lambda_{cloud}^{m}$.

79  The approach we use is to apply this definition to an elementary volume of cloud (volume outlined in red in Figure 1). This volume is bounded at its base by

80  an arbitrary section ($d\mathcal{S}$) aligned with the base of the cloud, with this volume extending vertically to the cloud summit.
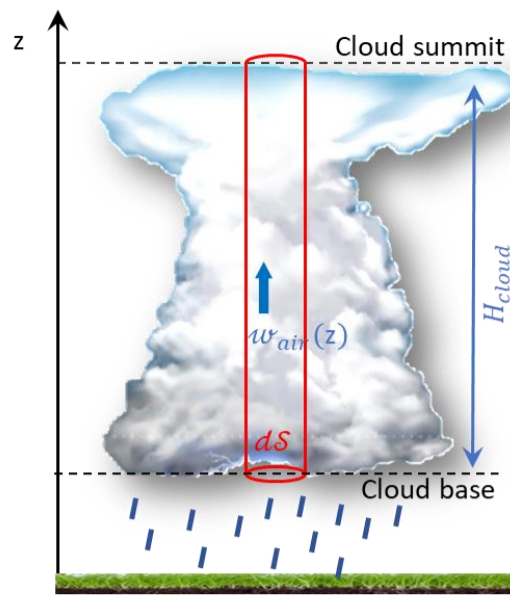
Figure 1. Definition of the scavenging coefficient at the scale of a cloud

In this elementary cloud volume, it is elementary to calculate the variation in the average mass concentration of aerosols of diameter $d_{ap}$, in relation to their transfer into precipitation:

$$dM(d_{ap}) = -\frac{\phi_{ap,precip}(d_{ap}).\, dS\, .dt}{dV_{cloud}} \qquad \text{Equation 2}$$

In this equation, $\phi_{ap,precip}(d_{ap})$ is the mass flow of dry particles of diameter $(d_{ap})$ leaving the cloud via precipitation (solids and liquids), and $dV_{cloud}$ is the elementary volume of cloud considered ($dV_{cloud} = H_{cloud}.\, dS$).

$$\Lambda^m_{cloud}(d_{ap}) = -\frac{1}{dt}\frac{dM(d_{ap})}{\langle M(d_{ap})\rangle}\Bigg|_{cloud} = \frac{\phi_{ap,\ precip}(d_{ap})|_{dS}}{\langle M(d_{ap})\rangle_{cloud}.\, H_{cloud}} \qquad \text{Equation 3}$$

In this equation, $\langle M(d_{ap})\rangle$ is the average mass concentration (over the thickness of the cloud) of dry particles of diameter $d_{ap}$. It is noteworthy that $\langle M(d_{ap})\rangle$ is not the average concentration of interstitial aerosols in the cloud but the average concentration of particles, which includes, in addition to the interstitial aerosols, all the particles included in the droplets and potentially in the ice phase. Thus, if we jointly determine $\langle M(d_{ap})\rangle$, $\phi_{ap,\ precip}$ as well as the thickness of the cloud $H_{cloud}$, it is possible to deduce a scavenging coefficient.

The average particle concentration is calculated, using Equation 4, by spatially averaging, over the entire thickness of the cloud, the concentrations of interstitial aerosols (of diameters $d_{ap}$) $M_{int}(z, d_{ap})$, the concentrations of particles in the drops $\left(\mathbb{M}(z, d_{ap})\right)$, and the concentrations in the ice phase $\left(\mathfrak{M}(z, d_{ap})\right)$.

$$\langle M(d_{ap})\rangle = \frac{1}{H_{cloud}}\int_{cloud\ base}^{cloud\ summit}\left(M_{int}(z, d_{ap}) + \mathbb{M}(z, d_{ap}) + \mathfrak{M}(z, d_{ap})\right)dz \qquad \text{Equation 4}$$

Finally, in order to evaluate the mass flow of particles exiting the cloud at its base $\left(\phi_{ap,\ precip}(d_{ap})\right)$, it is necessary to evaluate the cloud volume $(V(\mathcal{D}_{drop}))$ which contains all the droplets whose drop velocity $w_\infty(\mathcal{D}_{drop})$ is sufficient for them to pass through the section $dS$, during the time $dt$. Using the velocity composition law, we can deduce Equation 5.

$$V(\mathcal{D}_{drop}) = \max\left(0,\ w_\infty(\mathcal{D}_{drop}) - w_{air}(Z_{cloud\ base})\right).\, dS \qquad \text{Equation 5}$$

In this equation, $w_{air}(Z_{cloud\ base})$ is the velocity of the air parcel at the base of the cloud. By convention, $w_{air}$ is positive for an updraft and negative for a downdraft.

It is then immediately possible to deduce the flow of particles passing $dS$ through liquid precipitation:

$$\phi_{ap,\ rain}(d_{ap}) = \int_{d_{droplet}=0}^{\infty} \max\big(0,\ w_\infty(\mathcal{D}_{drop}) - w_{air}(Z_{cloud\ base})\big).\, \mathbb{M}(z, d_{ap}, \mathcal{D}_{drop}).\, d\mathcal{D}_{drop} \qquad \text{Equation 6}$$

106 In this equation, $\mathbb{M}\left(z, d_{ap}, \mathcal{D}_{drop}\right)$ is the concentration of particles contained in the droplets and of dry diameter $d_{ap}$.

107 The same applies to solid precipitation $\phi_{ap,\ ice}\left(d_{ap}\right)$ :

$$\phi_{ap,\ ice}\left(d_{ap}\right) = \int_{d_{ice}=0}^{\infty} \max(0,\ w_{\infty}(\mathbb{d}_{ice})$$
$$- w_{air}(z_{cloud\ base})).\mathfrak{M}\left(z, d_{ap}, \mathbb{d}_{ice}\right).d\mathbb{d}_{ice}$$

Equation 7

108 By adding these two flows together, it is possible to deduce the total flow of particles (of diameter $d_{ap}$) exiting the cloud through all precipitation:

109

$$\phi_{ap,\ precip}\left(d_{ap}\right) = \phi_{ap,\ rain}\left(d_{ap}\right) + \phi_{ap,\ ice}\left(d_{ap}\right)$$

Equation 8

110

111 Thus, to theoretically evaluate the cloud scavenging coefficient, it is first and foremost essential to be able to evaluate its contours, but also to be able to

112 determine the mass concentrations of particles in the droplets $\mathbb{M}\left(z, d_{ap}, \mathcal{D}_{drop}\right)$, in the ice phase $\mathfrak{M}(z, \mathbb{d}_{ice}, d_{ap})$, and in the interstitial aerosol $\mathcal{M}_{int}\left(z, d_{ap}\right)$.

113 To evaluate the contours of the cloud, it seems necessary in the first instance to consider once again its definition.

## 1.2. What is a cloud? (how to define its boundaries?)

115 The World Meteorological Organization defines clouds as: "an aggregation of minute particles of liquid water or ice, or of both, suspended in the atmosphere

116 and usually not touching the ground" (WMO, 2014). This definition would appear to be very inadequate for enabling the contours of a cloud to be

117 determined. Clouds, although very commonly talked about in everyday life and subject to numerous scientific studies, have contours that remain very

118 blurred. It is therefore always difficult to define them rigorously, and above all non-recursively. Spankuch *et al.,* (2022) further emphasised that, depending

119 on the scope of the authors' expertise (meteorology, climate, satellite observations, airborne, from ground radars, or using microphysical models), these

120 authors use significantly differing definitions and thresholds.

121 For example, Wood and Field, 2011 proposed criteria with respect to liquid water content (LWC), ice water content (IWC), or total concentrations in numbers

122 of hydrometeors (droplets and crystals).

123 Hiron (2018) proposed separating cloud water and precipitation water based on the criterion of the size of hydrometeors (hydrometeors with a diameter of

124 less than 64 µm are considered part of the cloud; larger than that are considered part of the rain); then, if the total cloud water content is greater than 0.1

125 g/cm$^3$, the air parcel is considered part of the cloud.

126 Other authors proposed contours based on relative humidity (Del Genio *et al.*, 1996) or total water content (TWC), whereas meteorologists and

127 climatologists tend to prefer optical thickness (Sassen and Cho, 1992), each with arbitrarily established thresholds.

128 Although these definitions can be linked mathematically to each other, these relationships are most often highly non-linear. Therefore, in this article, a

129 variety of cloud definitions will be considered, and we will examine the criteria that are most relevant for studying in-cloud scavenging and distinguishing it

130 from below-cloud scavenging. This relevance of the definition what constitutes a cloud will be analysed from two perspectives. Firstly, we consider a purely

131 physical perspective and, secondly, a more pragmatic perspective linked rather to applicability in an atmospheric dispersion model dedicated to crisis

132 management.

## 1.3. The DESCAM model

134 To simulate clouds of different types and theoretically evaluate their scavenging coefficient, it is necessary to have a model that makes it possible to simulate

135 all the water phase changes, considering the catalyst role of aerosols in most of these state changes (activation, ice nucleation, etc.). It is also necessary to

136 calculate the sink terms of interstitial aerosols (related to droplet collection or activation) and associate them with the source terms of particles in droplets

137 and ice, in order to calculate the mass of particles in droplets $\left(\mathbb{M}(d_{drop})\right)$ and in ice $(\mathfrak{M}(d_{ice}))$ throughout the simulation (Equation 6, Equation 7).

138 The DESCAM model meets these specifications. This detailed microphysical model classifies droplets $(\mathcal{D}_{drop} \in [1\ \mu m, 6.5\ mm])$, ice $(\mathbb{d}_{ice} \in$

139 $[1\ \mu m, 6.5\ mm])$, and aerosols $(d_{ap} \in [2\ nm, 12.7\ \mu m])$, each into 39 logarithmically distributed size classes. This makes it possible to explicitly monitor

140 their respective particle size distributions $\mathbb{N}(\mathcal{D}_{drop})$, $\mathfrak{N}(\mathbb{d}_{ice})$ and $\mathcal{N}(d_{ap})$, spatially and temporally. This model can be coupled with various dynamic models

141 that allow consideration of atmospheric flows. In this article, we will only consider a dynamic called 1D1/2 (Asai and Kasahara, 1967), implemented in the

142 DESCAM model by Monier, 2003. More realistic 3D dynamics (Clark and Hall, 1991) are implemented in DESCAM (Leroy 2007) but will not be considered in

143 this article.

144 **Description of the microphysical models modelled in DESCAM**

145 All the microphysical processes considered in the DESCAM model are presented in Figure 2.
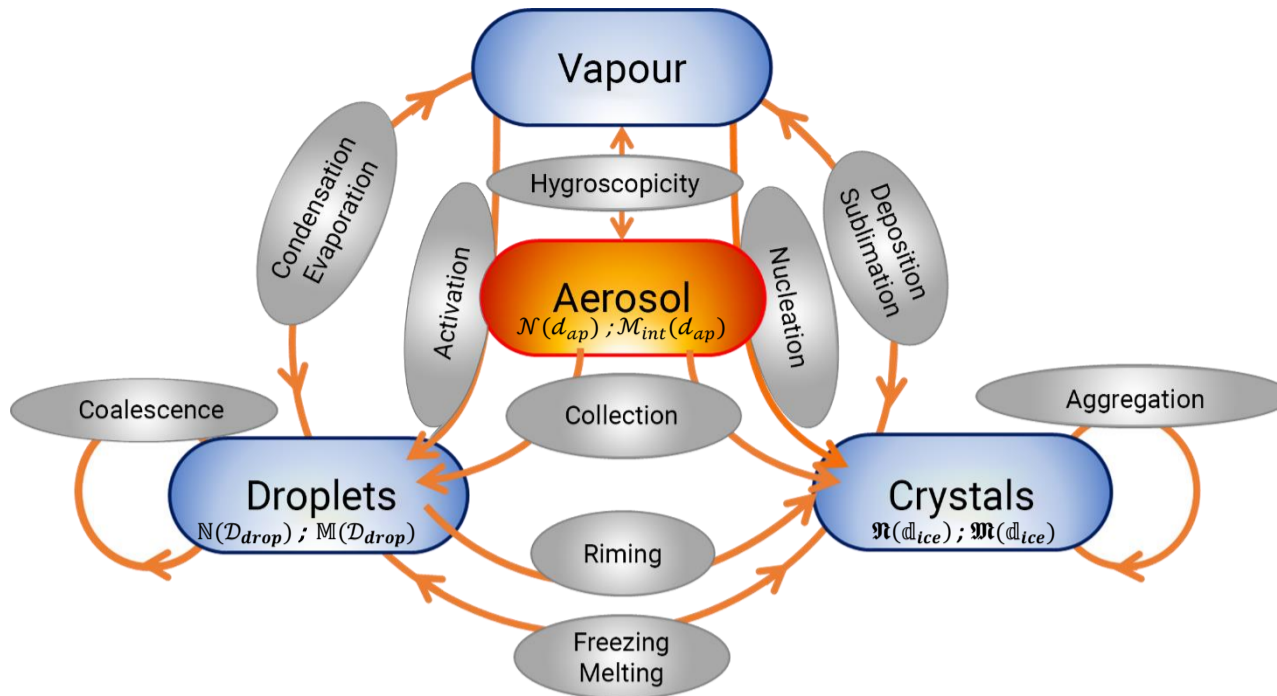
**Figure 2.** Modelling of microphysical processes in the DESCAM model.

In this figure, we can see the central role of aerosols in most water phase changes. The explicit resolution of all these microprocesses enables calculation of the particle size distributions of aerosols in each grid cell and at each time step (in number: $\mathcal{N}(d_{ap})$ (Equation 9) and in mass: $\mathcal{M}(d_{ap})$),) as well as the particle size distributions of the droplets (in number $\mathbb{N}(\mathcal{D}_{drop})$, Equation 10) and of the ice (in number $\mathfrak{R}(\mathbb{d}_{ice})$, Equation 11). In addition, in order to preserve the total mass of particles, the model also calculates two other quantities that are used to determine the masses of particles in droplets of diameter $d_{drop}$ $\left(\mathbb{M}(\mathcal{D}_{drop})\right)$, and in ice crystals of diameter $d_{ice}$ $\left(\mathfrak{M}(\mathbb{d}_{ice})\right)$.

$$\frac{d\mathcal{N}(d_{ap})}{dt} = \frac{d\mathcal{N}(d_{ap})}{dt}\bigg|_{dyn} + \frac{d\mathcal{N}(d_{ap})}{dt}\bigg|_{coll} + \frac{d\mathcal{N}(d_{ap})}{dt}\bigg|_{hygro} + \frac{d\mathcal{N}(d_{ap})}{dt}\bigg|_{act,\ deact} \qquad \text{Equation 9}$$

$$\frac{d\mathbb{N}(\mathcal{D}_{drop})}{dt} = \frac{d\mathbb{N}(\mathcal{D}_{drop})}{dt}\bigg|_{dyn} + \frac{d\mathbb{N}(\mathcal{D}_{drop})}{dt}\bigg|_{act,\ deact} + \frac{d\mathbb{N}(\mathcal{D}_{drop})}{dt}\bigg|_{coal}$$
$$+ \frac{d\mathbb{N}(\mathcal{D}_{drop})}{dt}\bigg|_{cond,\ vap} + \frac{d\mathbb{N}(\mathcal{D}_{drop})}{dt}\bigg|_{riming} + \frac{d\mathbb{N}(\mathcal{D}_{drop})}{dt}\bigg|_{frz,\ melt} \qquad \text{Equation 10}$$

$$\frac{d\mathfrak{R}(\mathbb{d}_{ice})}{dt} = \frac{d\mathfrak{R}(\mathbb{d}_{ice})}{dt}\bigg|_{dyn} + \frac{d\mathfrak{R}(\mathbb{d}_{ice})}{dt}\bigg|_{nucleation} + \frac{d\mathfrak{R}(\mathbb{d}_{ice})}{dt}\bigg|_{frz,\ sub} + \frac{d\mathfrak{R}(\mathbb{d}_{ice})}{dt}\bigg|_{agg}$$
$$+ \frac{d\mathfrak{R}(\mathbb{d}_{ice})}{dt}\bigg|_{riming} + \frac{d\mathbb{N}(\mathbb{d}_{ice})}{dt}\bigg|_{frz,\ melt} \qquad \text{Equation 11}$$

$$\frac{d\mathbb{M}(\mathcal{D}_{drop})}{dt} = \frac{d\mathbb{M}(\mathcal{D}_{drop})}{dt}\bigg|_{dyn} + \frac{d\mathbb{M}(\mathcal{D}_{drop})}{dt}\bigg|_{act,\ deact} + \frac{d\mathbb{M}(\mathcal{D}_{drop})}{dt}\bigg|_{coal}$$
$$+ \frac{d\mathbb{M}(\mathcal{D}_{drop})}{dt}\bigg|_{cond,\ vap} + \frac{d\mathbb{M}(\mathcal{D}_{drop})}{dt}\bigg|_{riming} + \frac{d\mathbb{M}(\mathcal{D}_{drop})}{dt}\bigg|_{frz,\ melt} \qquad \text{Equation 12}$$

$$\frac{d\,\mathfrak{M}(\mathbb{d}_{ice})}{dt} = \frac{d\,\mathfrak{M}(\mathbb{d}_{ice})}{dt}\bigg|_{dyn} + \frac{d\,\mathfrak{M}(\mathbb{d}_{ice})}{dt}\bigg|_{nucleation} + \frac{d\,\mathfrak{M}(\mathbb{d}_{ice})}{dt}\bigg|_{frz,\ sub} + \frac{d\,\mathfrak{M}(\mathbb{d}_{ice})}{dt}\bigg|_{agg}$$
$$+ \frac{d\,\mathfrak{M}(\mathbb{d}_{ice})}{dt}\bigg|_{riming} + \frac{d\,\mathfrak{M}(\mathbb{d}_{ice})}{dt}\bigg|_{frz,\ melt} \qquad \text{Equation 13}$$

In these equations, except for the index $\left(\ \big|_{dyn}\right)$ denoting variations due to atmospheric transport, each term corresponds to one of the microphysical processes outlined in Figure 2. For instance, $\left(\ \big|_{act,\ deact}\right)$ denotes to activation and deactivation processes. The subscripts $coll$, $hygro$, $frz$, $sub$, $coal$, $cond$, $vap$ and $agg$ respectively refers to the processes of aerosol collection by droplets, hygroscopicity of aerosol particles, freezing, sublimation,

coalescence, condensation, vaporization, and aggregation. The hygroscopic growth of aerosol particles is calculated assuming they are in thermodynamic equilibrium with the air supersaturation $S$ (Equation 14). This equilibrium is modelled after the $\kappa$-Köhler theory.

$$\frac{d\mathcal{N}(d_{ap})}{dt}\bigg|_{hygro} = \frac{\partial\mathcal{N}(d_{ap})}{\partial S}\bigg|_{\kappa-K\ddot{o}hler} \frac{\partial S}{\partial t}\bigg|_{dyn} \qquad \text{Equation 14}$$

Concerning the cold microphysics (Figure 2), this simulation integrates homogeneous freezing mechanisms (i.e., which do not require aerosol contribution) and heterogeneous freezing mechanisms (for which aerosols act as a catalyst for phase change). For homogeneous freezing, we consider the parametrisation of Koop *et al.,* (2000) adapted to DESCAM by Monier *et al.,* (2006). To model heterogeneous ice nucleation, we consider all the mechanisms described by Vali *et al.,* (2015). The Biggs formula (1953) is used to describe immersion freezing and the model of Meyers *et al.,* (1992) for condensation and contact freezing, as well as deposition nucleation. All these mechanisms have recently been incorporated into the DESCAM model by Hiron and Flossmann, (2015).

The main mechanism responsible for the flow of particles exiting the cloud via precipitation ($\phi_{ap,\,precip}(d_{ap})$, Equation 3) is activation. The collection of aerosols by droplets is only second order (Flossmann and Wobrock, 2010; Dépée, 2019). In the DESCAM model, activation is modelled by the $\kappa$-Köhler theory (Petters and Kreidenweis, 2007). This model makes it possible to determine equilibrium vapour pressure in the vicinity of a droplet of diameter $\mathcal{D}_{drop}$, as a function of the mass and type of solute (modelled by the $\kappa$ value) it contains, and therefore the supersaturation for this droplet. For a given mass and chemical nature of the pristine dry particle, one can compute the corresponding supersaturations for given size of solution droplets. This curve has a unique maximum, called critical supersaturation (Figure 3). The diameter associated with this critical supersaturation is called the activation diameter. Aerosols with a diameter smaller than the activation diameter are brought into thermodynamic equilibrium with their environment by hygroscopicity, with aerosols of a diameter greater than the activation diameter being converted into droplets and growing by means of vapour diffusion (by condensation).

In the DESCAM code, the microphysical process of collection (i.e. the process by which, during falling, droplets encounter impact and capture interstitial aerosol particles), is modelled in Equation 12 by the term $\frac{d\mathbb{M}(\mathcal{D}_{drop})}{dt}\big|_{coll}$ which is calculated by solving Equation 15. In this equation, the central term is the collection efficiencies $\left(E(d_{ap},\mathcal{D}_{drop},\mathcal{RH})\right)$. This is calculated by the model developed and validated by Dépée (Dépée *et al.*, 2019; Dépée *et al.*, 2021, Part I; Dépée *et al.*, 2020, Part II).

$$\frac{d\mathbb{M}(\mathcal{D}_{drop})}{dt}\bigg|_{coll} = \int_{d_{ap}=0}^{\infty} \mathcal{N}(d_{ap}) \frac{\pi\mathcal{D}_{drop}^2}{4} \mathcal{U}_{\infty,\,droplet}(\mathcal{D}_{drop}) E(d_{ap},\mathcal{D}_{drop},\mathcal{RH}) \frac{\pi d_{ap}^3}{6} \rho_{ap} \, dd_{ap} \qquad \text{Equation 15}$$

In this equation $\mathcal{U}_{\infty,\,droplet}(\mathcal{D}_{drop})$ corresponds to the terminal velocity of a droplet of diameter $\mathcal{D}_{drop}$ (calculated after the Beard (1973) model), $\rho_{ap}$ is the density of the aerosol particle, and $\mathcal{RH}$ refers to the relative humidity of air in the parcel.
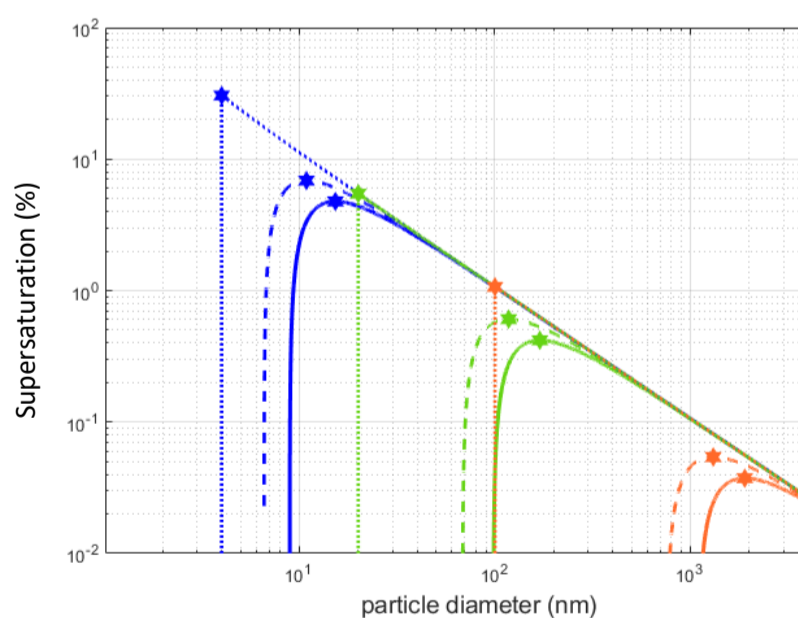
Figure 3. Thermodynamic equilibrium of an aerosol calculated as a function of particle diameter and nature of the initial dry particle. This calculation is made using the $\kappa$-Köhler theory (for a temperature of 293 K and a surface tension between solution and air of $72 \times 10^{-3}$ N.m$^{-1}$). (—) initial dry radius of the particles set at 4 nm; (—) initial dry radius set at 20 nm; (—) initial dry radius set at 100 nm; ( ··· ) $\kappa$ = 0, insoluble aerosol; (--) $\kappa$ = 0.61, moderately hygroscopic, as (NH$_4$)$_2$SO$_4$; (—) $\kappa$ = 1.28, highly hygroscopic, as NaCl; ✶ critical supersaturations needed to activate the aerosol and convert it into a cloud droplet.

193 Note that Equation 6 and Equation 7 are not directly calculable by the DESCAM model. This is because the model makes an inventory of the mass of particles

194 in the droplets and crystals according to the size of the hydrometeors ($\mathbb{M}(\mathcal{D}_{drop})$, Equation 12 and $\mathfrak{M}(\mathbb{d}_{ice})$, Equation 13), but without memorising the size

195 of the aerosols before their incorporation. The scavenging coefficients calculated in this article are therefore averaged, in mass, over the particle size

196 distribution of the aerosols. In this article we focus on validating the approach described by applying it to different types of cloud. Current work and future

197 publications will focus on demonstrating that the scavenging coefficient may be simply spectrally calculated, without modifying the model.

198

### Modelling of atmospheric dynamics

200 As stated previously, in this article we have limited our study to the 1.5D Dynamic framework developed by Asai and Kasahara, (1967). This has been regularly

201 used (Monier *et al*., 2005; Leroy *et al.,* 2006; Quérel *et al*., 2014; Hiron & Flossmann, 2015) to study the microphysical processes involved in the life cycle of

202 cumulus clouds. This model considers two concentric cylinders. The inner cylinder has a radius 10 times smaller than the outer cylinder. In the inner cylinder,

203 the vertical velocity of the flows is determined by solving a simplified form of the Navier-Stokes equations, coupled with the energy conservation equation.

204 The outer cylinder serves primarily for guaranteeing the condition of zero velocity divergence (continuity equation for incompressible flow). To this end, a

205 radial velocity component is introduced at the interface between these two cylinders (hence the expression of a 1.5D model), calculated from the

206 convergence or divergence layers and allowing entrainment from the environment. In this environment the only variable updated in this outer cylinder is

207 the vertical velocity to evaluate the radial gradient in vertical velocity and the subsequent turbulent flux; all the other variables are assumed to be unaffected

208 by the cloud processes within the inner cylinder and kept constant throughout the simulation.

209 All the microphysical processes detailed in the previous section and summarised in Figure 2 are calculated only in the central cylinder. Thus, this is also in

210 the inner cylinder, for each grid layer, that phase changes in the water will be computed with the subsequent absorption or release of latent heat that will

211 alter the buoyancy of the air and which ultimately generate the updraft and downdraft motions.

## 2.  Application to example cloud types

213 To establish a theoretical scavenging coefficient scheme, the methodology described above is applied to two very different idealised case studies

214 representative of two different types of clouds. First, we will model a vigorous cumulonimbus, then a shallow stratus. These two cloud types were selected

215 as they present, respectively, the higher and lower values, in terms of vertical extension, relative humidity, and rainfall intensity. Furthermore, while the

216 stratus that we simulate is shallow enough to be a warm cloud, cold microphysical processes are essential to capture the development of the cumulonimbus

217 situation.

218

### 2.1.Application to a cumulonimbus

### Description of the cumulonimbus considered

221 The cloud selected to model the cumulonimbus is the episode of 19 July 1981 of the CCOPE campaign (Cooperative Convective Precipitation Experiment;

222 Knight 1982 and Dye *et al.,* 1986), which took place near Miles City in Montana (USA). This episode was selected because it is very finely documented and

223 this episode is a test case for many codes simulating the formation of convective clouds, and in particular the DESCAM model (Flossmann & Wobrock, 2010).

224 A radio sounding taken at Miles City at 16h00 local time (just before the storm) is used to initialise the thermodynamic conditions of the atmospheric column:

225 temperature and humidity. For the vertical pressure profiles, standard conditions are assumed. In addition, we used the observations of both two Doppler

226 radars measured high-resolution reflectivity as well as the movements of the cloud and five aircrafts that were able to make numerous passes through the

227 cloud throughout its maturation and through to the precipitation episodes. The spatial-temporal evolution of the thermodynamic conditions, associated

228 with the microphysical properties of the cloud system, and the atmospheric flows are therefore recorded in fine detail for the entire life of this cumulonimbus

229 and can be used to evaluate the model performance to capture the clouds physics. For this article, we therefore used the same modelling hypotheses as

230 those detailed by Leroy *et al.,* (2006). Convection was triggered by +2.3°C heating of the ground during the first 10 minutes of the simulation. During this

231 campaign, no physicochemical measurements were made of the aerosols, hence we consider that they consisted of ammonium sulfate ($\kappa = 0.61$ and $\rho_{dry} =$

232 $1.77 \cdot 10^3$ kg.m$^{-3}$ Petters and Kreidenweis, 2007) with an initial particle size distribution of the Jaenicke continental type (1988). We considered a homogeneous

233 distribution in the atmospheric boundary layer (i.e., over the first 3 kilometres), then above the concentration is assumed to decrease exponentially with a

234 scale height of 3000 m (Figure 4).

235
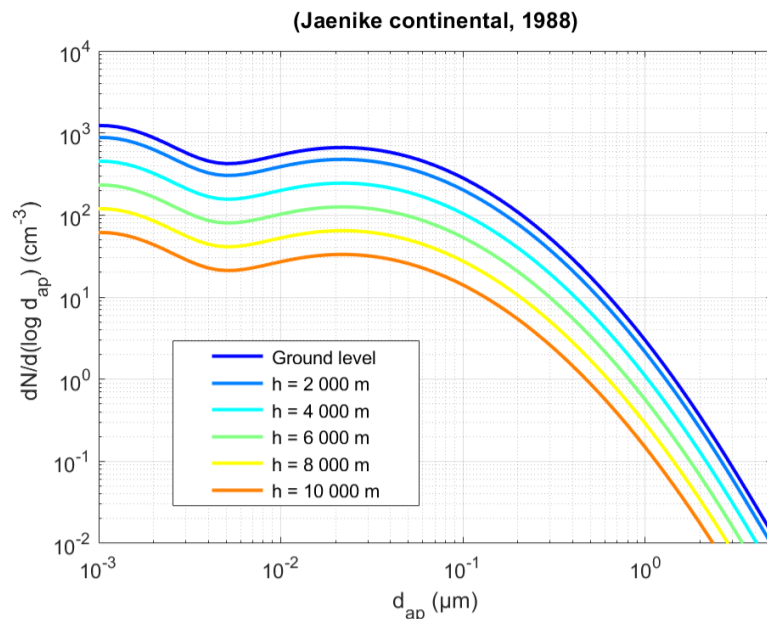
236                         Figure 4. Initial particle size distribution of aerosols considered for this simulation.

237      The simulation lasted 3600 s, on a 10 km high column. The spatial and temporal resolutions were set to 100 m and three seconds respectively.

238      Figure 5 and Figure 6 show respectively the spatial-temporal evolutions of the vertical flows in the central cylinder and the liquid water and ice content.
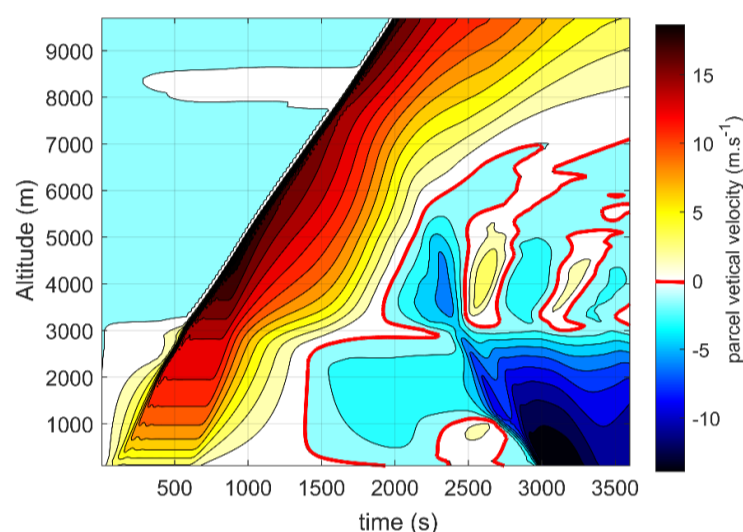
239

240     Figure 5. Spatial-temporal distribution of the vertical components of atmospheric flows. The thick line in red separates the updraft ($w_{air} > 0$) flows from
241                                         the downdraft flows ($w_{air} < 0$).

242      In these figures, we can see that the initial superheating of the air layer at ground level induces an updraft flow due to buoyancy forces. Approximately 500 s

243      after the start of the simulation, the air reaches critical supersaturation at an altitude of 3000 m and the aerosols are gradually converted into droplets. The

244      spatial-temporal distribution shown on the left of Figure 6 highlights the appearance of a cloud at the spatial-temporal coordinate (500 s, 3000 m). Vapour

245      condensation induces a latent heat release, which in turn increases buoyancy of the air parcel, accelerating the updraft flows (approx. 15 m.s⁻¹ at 4000 m).

246      This flow transports the vapour at altitude and by cooling this induces the progressive activation of the aerosols, and a vertical extension of the cloud. Near

247      7000 m, the first ice crystals are formed. The coexistence of ice crystals and supercooled droplets will allow rapid crystal growth with a corresponding

248      reduction of liquid water content (best known as the WBF process for: Wegener, 1911; Bergeron, 1928; Findeisen, 1938). Then, the crystals begin to

249      precipitate at around 1700 s since they reach sizes large enough for their gravitational settling velocity to supersede updraft speed. In precipitating, the

250      larger crystals collect the suspended droplets. Hence, under the coupled influence of the WBF process and, above all, the collection of droplets by the ice

251      particles, after 2200 seconds of simulation the cloud only contains ice. Finally, below an altitude of 3000 m, the solid hydrometeors melt and liquid

252      precipitation forms. Figure 6 shows on the right the rainfall intensities, as well as the cumulative precipitation calculated by the model at ground level. This

253      timeline presents two local maxima: the first at 2750 s after the start of the simulation, corresponding to an intensity of 18 mm.h⁻¹ and the second 300 s

254      later, with an intensity of about 46 mm.h⁻¹.
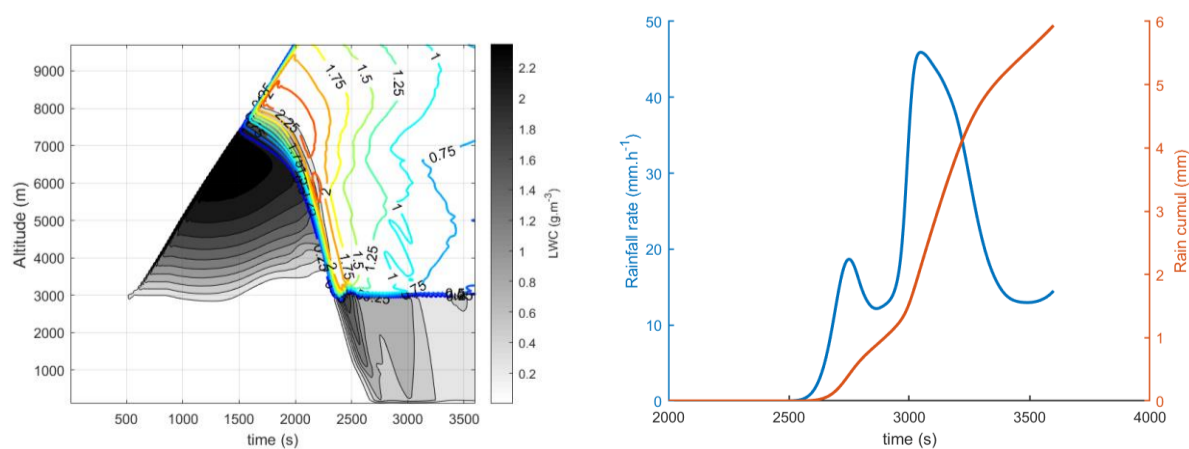
255

256          Figure 6. On the left: Spatial-temporal distributions of liquid water content (LWC, greyscale) and ice content (IWC, iso-contours).
257                 On the right: Temporal evolution of rainfall intensity and cumulative precipitation at ground level

**Calculation of the scavenging coefficient**

258 Based on this modelling results, we applied all the methodology described in section 1.1. The first step consisted in establishing the contours of the cloud,

259 in order then, using Equation 3 integrated over the entire aerosol distribution, to be able to calculate the equivalent cloud scavenging coefficient.

260

$$\Lambda_{cloud}^m = -\frac{1}{dt}\frac{d\mathcal{M}}{\langle\mathcal{M}\rangle}\bigg|_{cloud} = \frac{\phi_{ap,\ precip}}{\langle\mathcal{M}\rangle.\ H_{cloud}} \qquad\qquad \text{Equation 16}$$

261 As already indicated in section 1.2, there is no strict definition of the boundaries of the cloud, particularly at the interface with the precipitation, and it can

262 also be observed in Figure 6 that the total water content does not show any demarcation between the cloud and the precipitation. Moreover, as Spänkuch

263 *et al.*, (2022) point out, the physical phenomenon studied will determine which contours are the most relevant. Therefore, for this study, we examined three

264 of the physical parameters to establish this contour. These three criteria are the relative humidity of the air parcel (calculated in relation to liquid water),

265 the mass concentration of hydrometeors with a diameter of less than 64 µm and, lastly, the concentration of hydrometeors. The contours of this

266 cumulonimbus are presented in Figure 7 for each of these criteria, each with two thresholds considered. The thresholds levels were chosen arbitrarily, mainly to

267 observe their influence on scavenging when they vary over wide ranges of values.
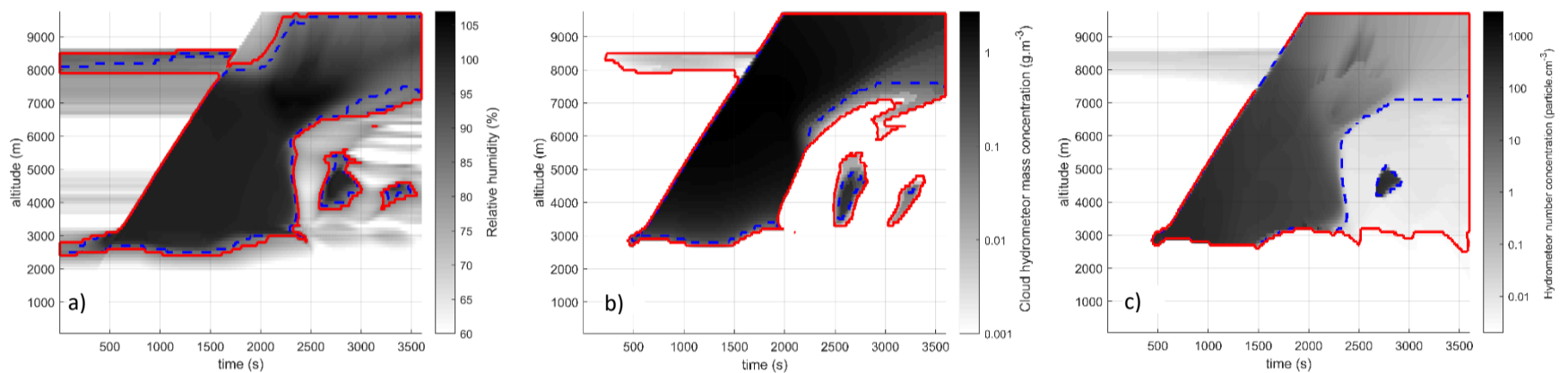
268

269 Figure 7. Test of different criteria to establish the contours of the simulated cumulonimbus.
270 a) threshold based on relative humidity: (- - -) $RH > 85\%$; (—) $RH > 80\%$.
271 b) threshold based on the total water content of hydrometeors with a diameter less than 64 µm: (- - -) mass concentration of cloud
272 hydrometeors $> 0.1\ g.m^{-3}$ ; (—) mass concentration of cloud hydrometeors $> 0.001 g.m^{-3}$.
273 c) threshold based on number concentration of total hydrometeors: (- - -) $\int d\mathbb{N} + d\mathfrak{R} > 0.03\ cm^{-3}$
274 (—) $\int d\mathbb{N} + d\mathfrak{R} > 0.003\ cm^{-3}$

275 We can see in this figure that, apart from the criterion based on the concentration of hydrometeors (Equation 9), with a threshold of 0.003 hydrometeors

276 per cubic centimetre, all the other criteria yield very similar contours. Thus, the cloud forms close to an altitude of 3000 m and its base remains constant for

277 up to 2500 s of simulation. During these 2500 s, the cloud thickens vertically until it reaches the tropopause (considered to be at 10,000 m in this calculation).

278 As shown in Figure 6 (on the right), 2500 s corresponds to the start of precipitation. This moment corresponds to an elevation of the base of the cloud up to

279 about 7000 m, except for the last criterion ($\mathcal{N}_{hydrometeor} > 0.003\ cm^{-3}$), for which the height of the base of the cloud remains constant close to the

280 altitude of 3000 m, even during rain.

281 Initially, our objective was to find a bijective relationship between a set of meteorological parameters available in DESCAM and the scavenging coefficient

282 calculated by this methodology. The reason for a bijective relationship is twofold, first it ensures a better robustness of the model, second it allow to perform inverse

283 calculation to estimate the discharge in case of ground contamination.

284 Most often in the literature, cloud scavenging is described as a power function of precipitation intensity (Hertel *et al.*, 1995; MRI, 2015; Leadbetter *et al.*,

285 2015; Groell *et al.*, 2014; Quérel *et al.*, 2021). Figure 8, Figure 9 and Figure 10 respectively present the contours of the cloud established on the basis of the

286 three criteria previously introduced (Figure 7). Within these contours, we calculated the total mass concentration of ammonium sulfate ($\mathcal{M}(z)$), adding

287 together the respective concentrations of the aerosol phases ($\mathcal{M}_{int}(z)$), in the droplets ($\mathbb{M}(z)$) and in the crystals ($\mathfrak{M}(z)$). Knowing the flux of ammonium

288 sulfate that is within the precipitative hydrometeors through the base of the cloud (Equation 6, Equation 7 and Equation 8), we could deduce the scavenging

289 coefficient, which we plotted according to the precipitation intensity calculated at the base of the cloud. Like Costa *et al.,* (2010), Stephan *et al.,* (2008) and

290 Quérel *et al.* (2021), a threshold of 0.1 mm.h $^{-1}$ was considered to limit noise. In Figure 8, 9, 10, the correspondence of the dots can be deduced with the

291 colour codes of the points. On the left-hand side, the identification of the spatial-temporal coordinates where precipitation and scavenging coefficient are

292 calculated is plotted. On the right-hand side, the corresponding relationship between scavenging coefficient and precipitation intensity can be read. These

293 results are of great importance because they show that the relationship between the scavenging coefficient and the rainfall intensity is the same at the

294 beginning and the end of the rainfall episode. In addition, an adjustment by a power law is determined for each contour. The coefficients for these

295 adjustments are shown in Table 1.

296
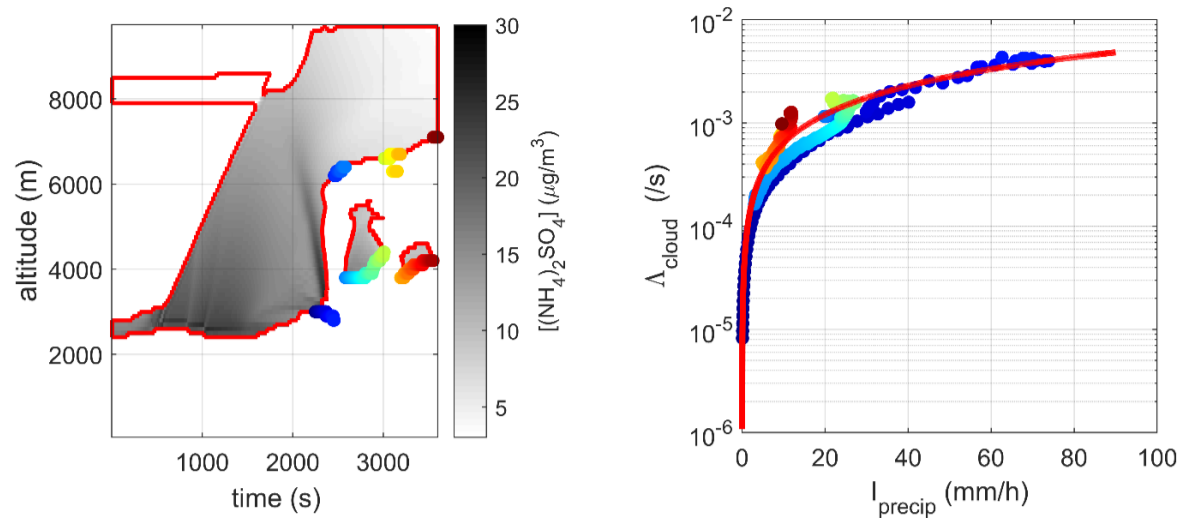
Figure 8. On the left: spatial-temporal distribution of the ammonium sulfate concentration in the cloud contour (—cloud contour for a relative humidity greater than 80%). On the right: correlation between the scavenging coefficient and the precipitation intensity determined at the base of the cloud, (—) adjusted by a power law.

300
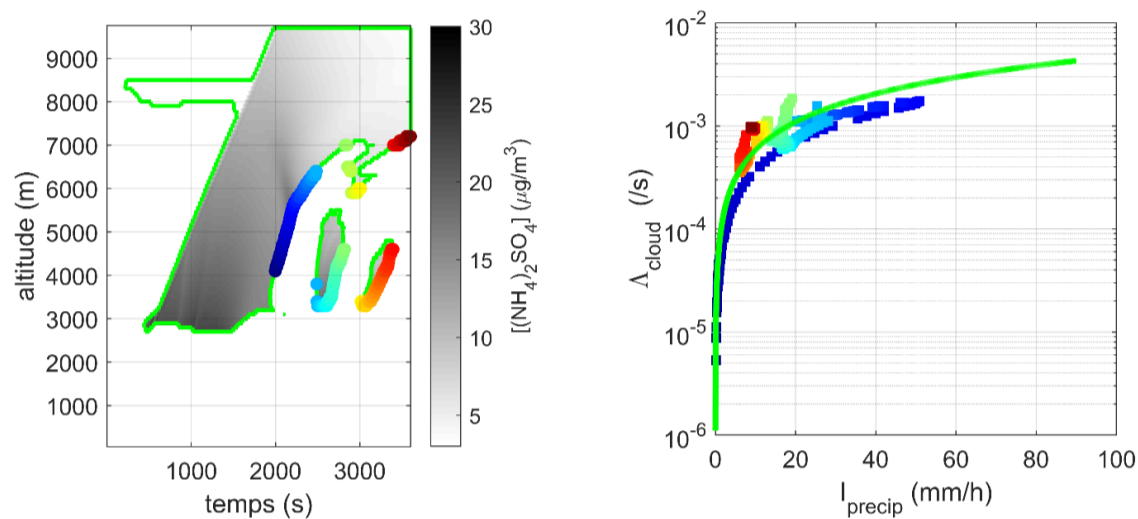
Figure 9. On the left: spatial-temporal distribution of the ammonium sulfate concentration in the cloud contour (— cloud contour for a mass concentration of cloud hydrometeors greater than 0.001 g.m$^{-3}$). On the right: correlation between the scavenging coefficient and the precipitation intensity determined at the base of the cloud, (—) adjusted by a power law.

304
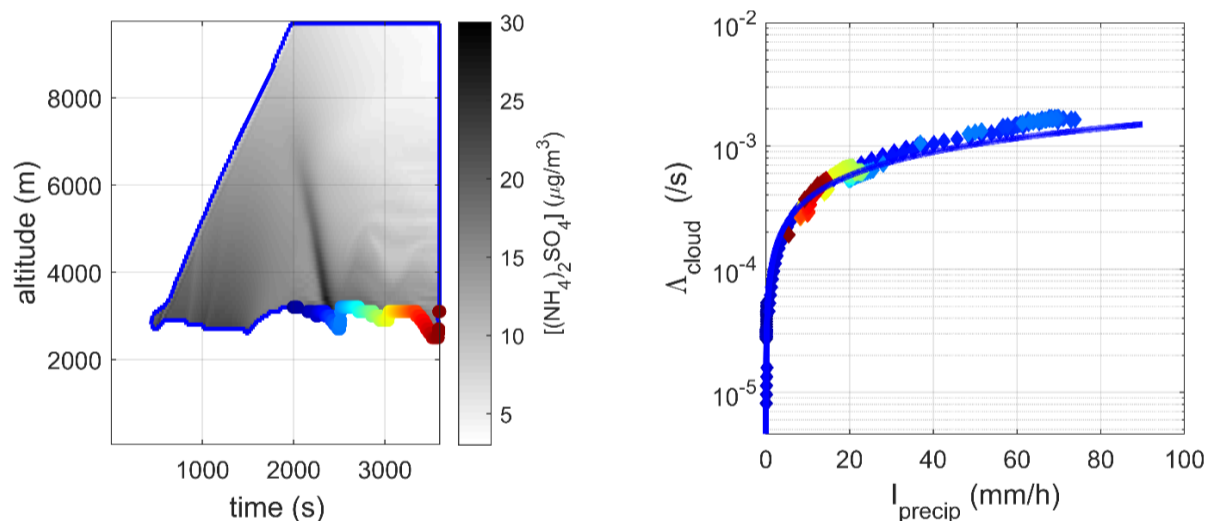
Figure 10. On the left: spatial-temporal distribution of the ammonium sulfate concentration in the cloud contour (— cloud contour for a concentration in number of hydrometeors greater than 0.003 particles.cm$^{-3}$). On the right: correlation between the scavenging coefficient and the precipitation intensity determined at the base of the cloud, (—) adjusted by a power law.

308

In these three figures, we observe that the relationship linking the intensity of precipitation to the scavenging coefficient by the cloud is fairly insensitive to the definition selected to describe its contour. Moreover, the power law adjustments plotted in Figure 8, Figure 9 and Figure 10 are very similar (Table 1). Nevertheless, only the last contour, based on the hydrometeor concentration (and with a threshold of 0.003 cm$^{-3}$), gives a perfectly bijective relationship between the precipitation intensity at the base of the defined contour and the scavenging coefficient. This result is surprising because, as previously mentioned in section 1.3, the driving mechanism for in-cloud scavenging is dominated by the activation (which is driven by the supersaturation level and physical-chemical properties of the aerosols, Flossmann and Wobrock, 2010). It would therefore seem logical that a criterion based on the relative humidity in the grid cell would be the most relevant. However, it is the criterion based on the concentration of hydrometeors that is the more reliable. This is because there are zones in the cloud where the humidity is too low to activate the aerosols (e.g., at 4000 m at 2500 s where RH <85%, or indeed Figure 7a), but where there is a significant number of droplets and crystals (> 0.03 cm$^{-3}$). These droplets and crystals have been activated elsewhere and previously, but they nevertheless continue to collect aerosols around them – for example by Brownian capture, contributing to scavenging. It therefore justifiable to define a cloud contour based on a diagnostic of the numeric concentration of hydrometeors.

 Table 1: Power law adjustment associated with each of the cloud contours studied.

| Contour type | Power law adjustments |
|---|---|
| **Based on relative humidity** (Figure 8) | $\Lambda_{cloud}^m = 7.6 \times 10^{-5} I^{0.92}$ |
| **Based on mass concentration of cloud** hydrometeors (Figure 9) | $\Lambda_{cloud}^m = 7.2 \times 10^{-5} I^{0.9}$ |
| **Based on numeric concentration of** hydrometeors (Figure 10) | $\Lambda_{cloud}^m = 8.6 \times 10^{-5} I^{0.6}$ |

322

323 However, this numeric concentration criterion, although more precise for theoretically assessing the scavenging coefficient, is not easily accessible in a crisis
324 code. Nevertheless, detailed analysis of the results of these simulations seems to show that it would be wise to define the cloud base as being constant and
325 equal to the altitude at which critical supersaturation was first reached, i.e., the altitude at which the cloud began its formation.

326

### 2.2. Application to a stratus

**Description of the stratus considered**

329 The same approach as above was considered for modelling scavenging by a shallow stratus cloud. The main differences with the previous modelling (i.e., of
330 the cumulonimbus) beyond the initialisation of thermodynamical profile is the treatment of the vertical advection within the cloud. Whereas, for the
331 previous modelling, differences in air buoyancy (related to the initial thermal gradients and latent heat released by water phase changes) were the cause of
332 vertical velocities and could be described and captured by the dynamics of the model. When it comes to modelling stratus clouds, the dynamics are governed
333 by large scales features that are not included in the 1.5D model. Therefore, the idea is to completely prescribe the time evolving profile for vertical velocity
334 to model this forcing. Since convection is forced rather than triggered by buoyancy, it's reasonable to prescribe it and not calculate the microphysical
335 feedback on dynamics. For the scenario, we considered the vertical advection model proposed by Zhang *et al.,* (2004) and recapitulated in Equation 17. We
336 therefore imposed a sinusoidal profile vertical velocity, the maximum oscillating from positive to negative values with a period of 1800 s. The maximum of
337 the velocities was located at the altitude ($z_c$) of 1000 m and vertical motions allowed between 700 and 1300 m ($h_c$ = 600 m, Figure 11). Like Zhang *et al.,*
338 (2014), in the advection model, we imposed an average updraft velocity ($w_0$) of 0.2 m.s$^{-1}$ and an oscillation amplitude ($w_1$) of 0.8 m.s$^{-1}$ at an altitude of
339 1000 m. Figure 5 shows the spatial-temporal distribution of vertical flows prescribed in the central cylinder. The temperature profile follows a dry adiabatic
340 lapse rate with a temperature of 15°C on the ground so that there are no negative temperatures in the cloud. Above 1300 m, like Zhang *et al.* (2014), we
341 imposed an inversion of the thermal profile. At altitudes between 700 and 1300 m, the relative humidity was initialised at 98.5%, and 95% outside of this
342 range. For the aerosols, the initial conditions were identical to those for cumulonimbus (Equation 5).

$$
\begin{cases}
w(z,t) = \cos\left(\pi \frac{z-z_c}{h_c}\right)\left[w_0 + w_1 \sin\left(\frac{2\pi t}{t_c}\right)\right] & if \ |z-z_c| \leq \frac{h_c}{2} \\
w(z,t) = 0 & if \ |z-z_c| > \frac{h_c}{2} \\
z_c = 1000 \ m; \ h_c = 600 \ m; \ t_c = 1800 \ s; \ w_0 = 0.2 \ m.s^{-1}; w_1 = 0.8 \ m.s^{-1}
\end{cases}
\qquad \text{Equation 17}
$$

343
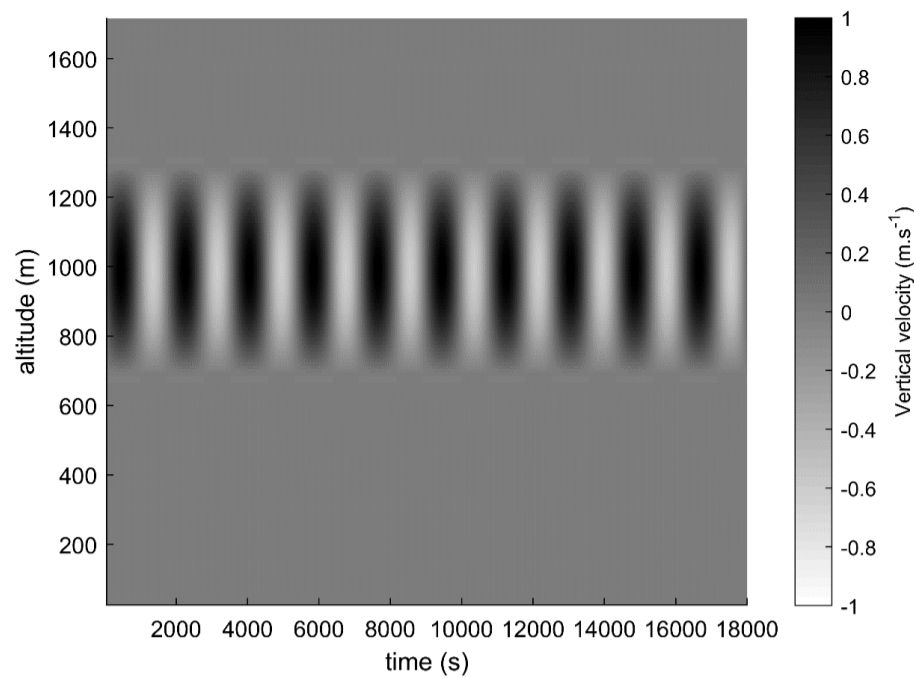
Figure 11. Spatial-temporal distribution of the vertical components of atmospheric flows (Zhang *et al.*, 2004)

Figure 12 shows on the left the spatial-temporal distribution of the water content calculated by DESCAM. The critical supersaturation was reached close to the altitude of 700 m from the first updraft phase (0–1000 s). The LWC then increased with altitude throughout the phase where the atmospheric flows were ascending. At the cloud summit, the liquid water content reached approximately 1.6 g.m$^{-3}$. Conversely, during the downdraft phases, the supply of dry air to lower altitudes induced, due to the temperature profile considered, a drop in the relative humidity occurs, which in turn induced evaporation of the droplets, resulting in a significant reduction in the LWC. These downdraft phases also had the effect of advecting droplets below the cloud band. During the period of velocity oscillations ($t < t_c$), precipitation completely evaporated before reaching the ground. However, from the second period onwards, rain was diagnosed at ground level (Figure 6. b).

352
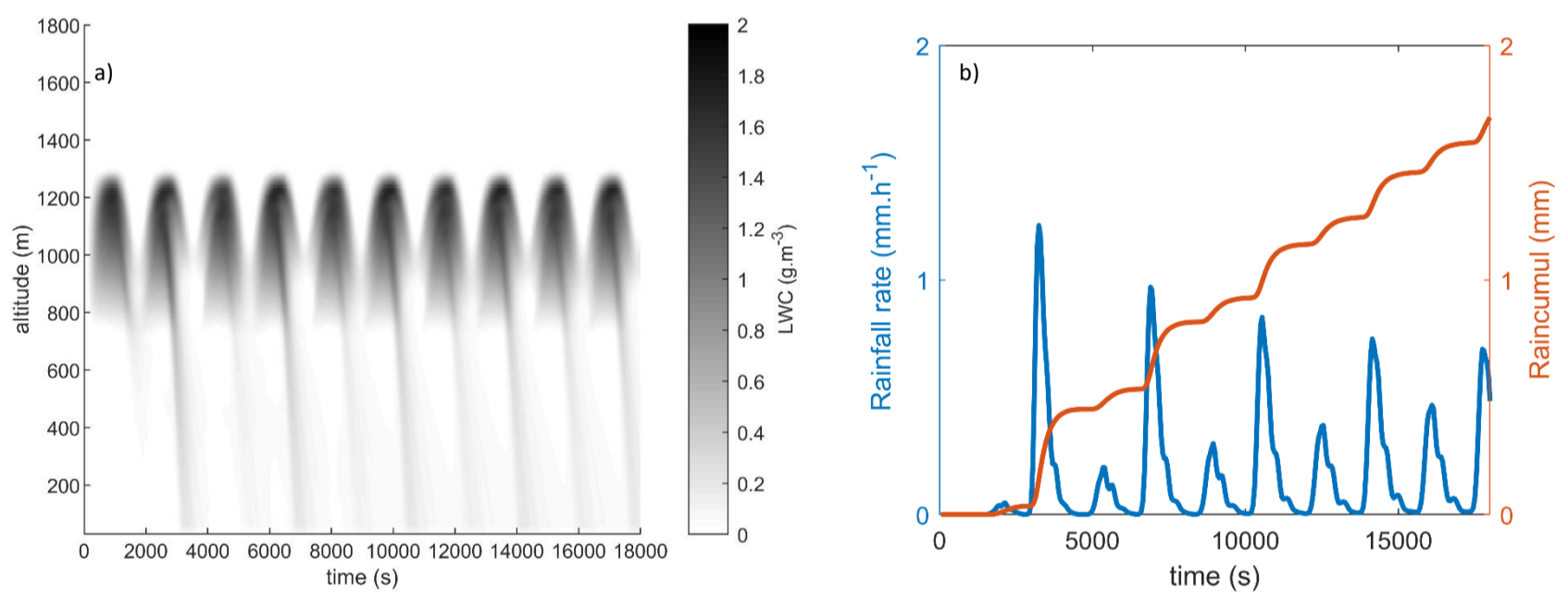
Figure 12. On the left: Spatial-temporal distribution of the liquid water content calculated by DESCAM (LWC, in greyscale).
On the right: Temporal evolution of rainfall intensity and cumulative precipitation diagnosed by DESCAM at ground level.

The DESCAM model predicts intermittent precipitation at ground level with flurries of precipitation in the order of a millimetre per hour. Over a precipitation period of approximately four hours, the cumulative precipitation was only approximately 3 mm.

357

### Calculation of the stratus scavenging coefficient

As before in the case of cumulonimbus, it is necessary to define the contours of the cloud. We therefore used the three criteria previously introduced and look for the one with the clearest demarcation line between the cloud zone and the precipitation zone, to apply a dedicated scavenging coefficient (Figure 13). As before, we observe from Figure 12.a that water content is not a good indicator to outline the cloud boundaries. Indeed, no discontinuity is observed for this parameter enabling demarcation between the cloud and the precipitation.

363
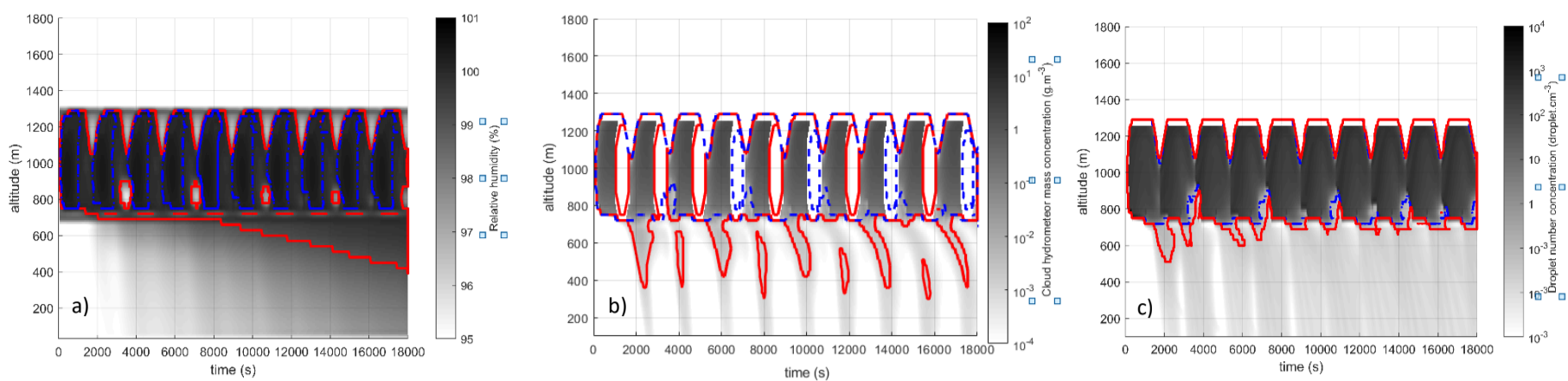
Figure 13. Test of different criteria to establish the contours of the simulated stratus.

a) threshold based on relative humidity: ($- - -$) $RH > 99\%$; (—)$RH > 100\%$.

b) threshold based on the mass concentration of hydrometeors with a diameter less than 64 μm: (---) mass concentration of cloud hydrometeors $> 0.01\ g.m^{-3}$ ; (—) mass concentration of cloud hydrometeors$> 0.001 g.m^{-3}$;

c) threshold based on the concentration of hydrometeors: (---); $\int d\mathbb{N} > 0.1\ cm^{-3}$ ; (—) $\int d\mathbb{N} + d\mathfrak{N} > 0.03\ cm^{-3}$.

Based on these results, it is more difficult to delineate the contours of this stratus than for the cumulonimbus. This is because, for these three criteria, only the droplets concentration shows a clear demarcation between precipitation and cloud zone. Moreover, only this criterion gives stable cloud contours, regardless of the threshold value selected. This difference with respect to the cumulonimbus is mainly due to the size of the precipitating hydrometeors, which are much larger in the case of cumulonimbus. Figure 14 shows that the particle size distribution mode in number of raindrops, for the cumulonimbus, is close to a diameter of 1 mm, whereas it is 100 μm for the stratus. It is therefore easier with a cumulonimbus than with a stratus to define a size threshold distinguishing droplet (belonging to the cloud) from raindrops (belonging to precipitation). The criterion based on the mass concentration of hydrometeors exceeding 64 μm is therefore less effective under a stratus than under a cumulonimbus. To explain the poor performance of the criterion based on relative humidity, again it is the particle size that counts. As the droplets under the stratus are smaller than under the cumulonimbus, their velocities are lower, and they reside longer in the atmosphere – about 10 times longer. This longer residence time promotes the increase in relative humidity under the cloud, and humidity saturation under the cloud. This makes it difficult to use this criterion to determine the boundary between rain and cloud for a stratus.
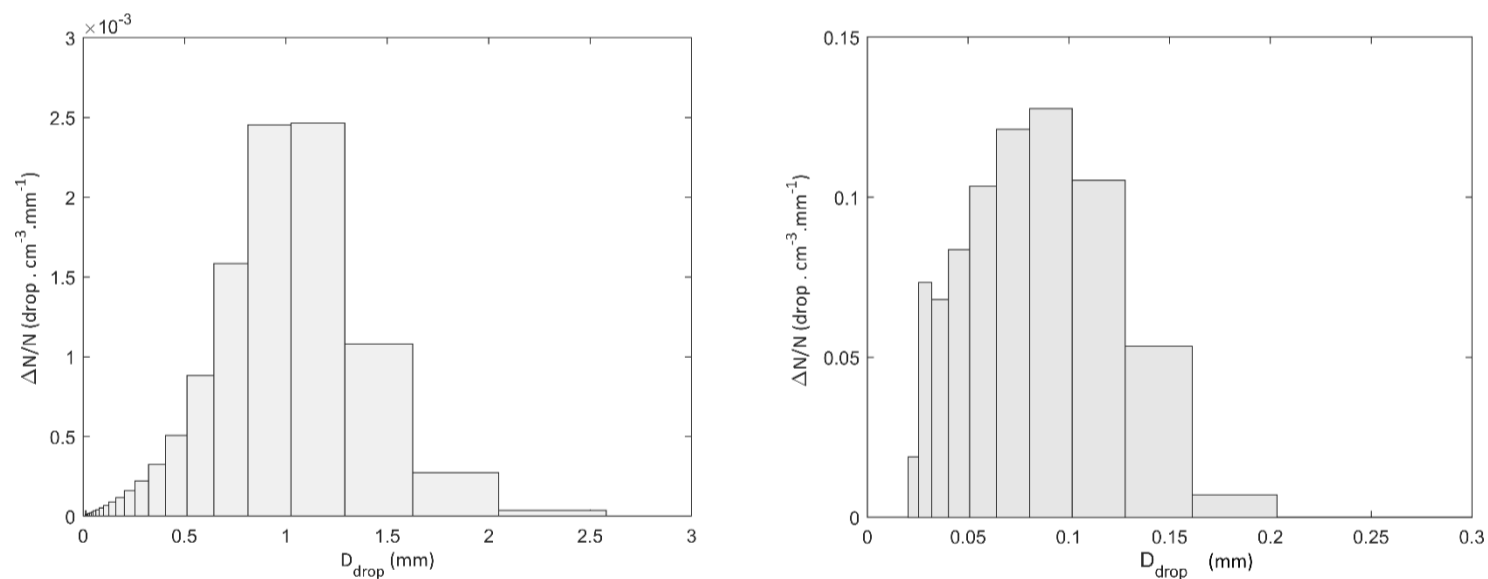
381

Figure 14. Particle size distributions of raindrops determined by the DESCAM model at ground level

Left: For cumulonimbus at time t=3000 s

Right: For cumulonimbus at time t=8200 s

As previously, for the cumulonimbus, we search for a criterion to delimit cloud from rain. The same parameters as in section 2.1 are investigated and presented in Figure 15, 16 and 17.

388
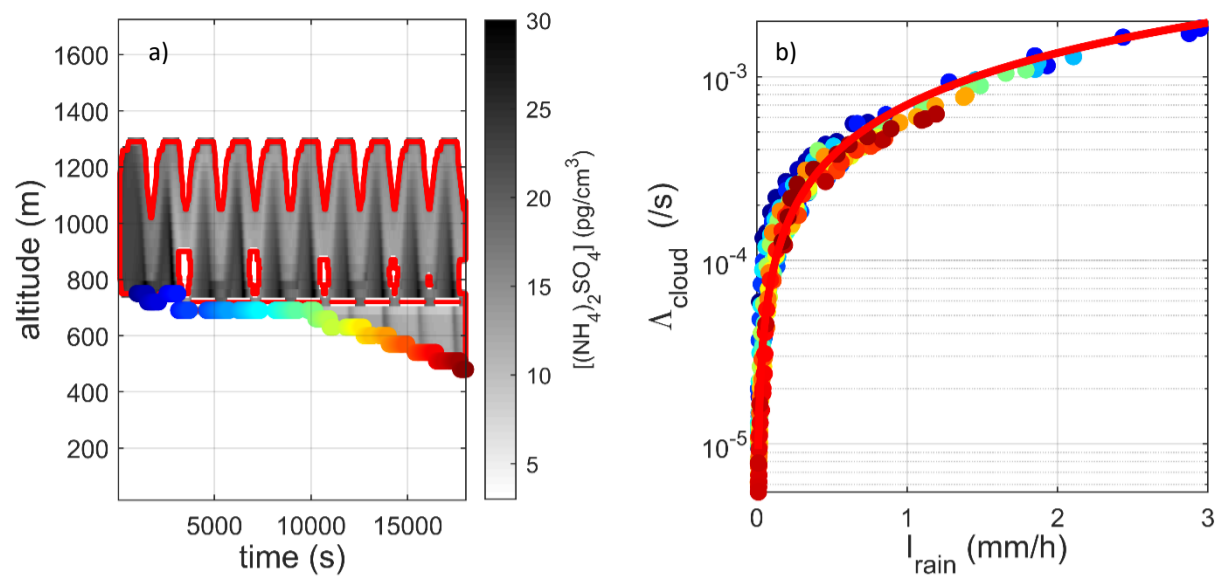
Figure 15. On the left: spatial-temporal distribution of the ammonium sulfate concentration in the cloud contour (—cloud contour for a relative humidity above 99%). On the right: correlation between the scavenging coefficient and the precipitation intensity determined at the base of the cloud, (—) adjusted by a power law.

392
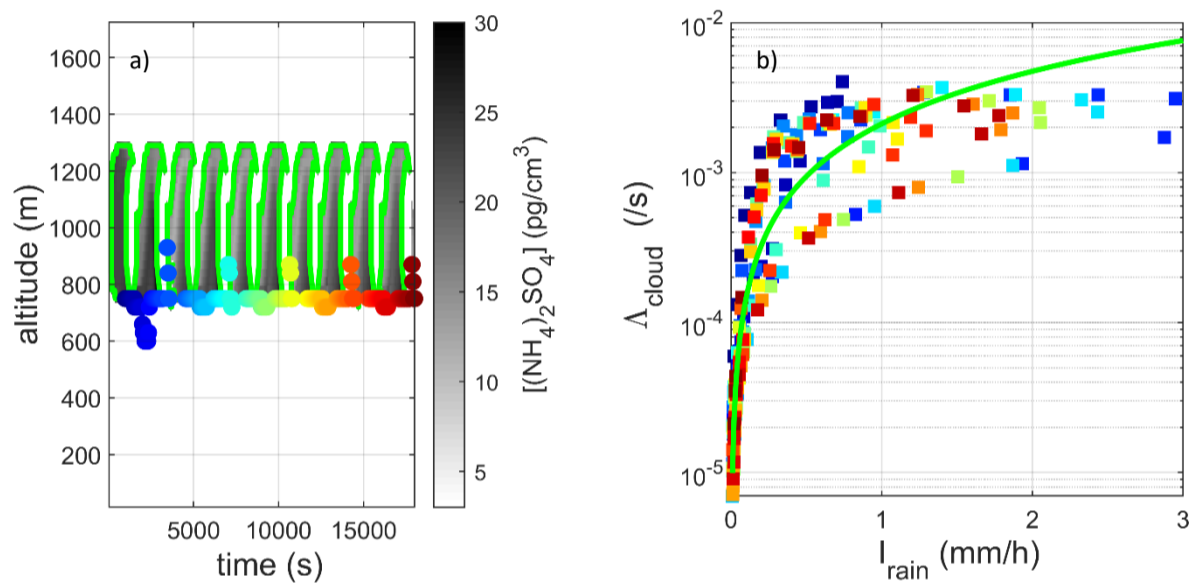
Figure 16. On the left: spatial-temporal distribution of the ammonium sulfate concentration in the cloud contour (— ) criterion based on the mass concentration of hydrometeors with a diameter greater than 64 µm with a threshold set at 0.01 g.m$^{-3}$). On the right: correlation between the scavenging coefficient and the precipitation intensity determined at the base of the cloud, (— ) adjusted by a power law.

396
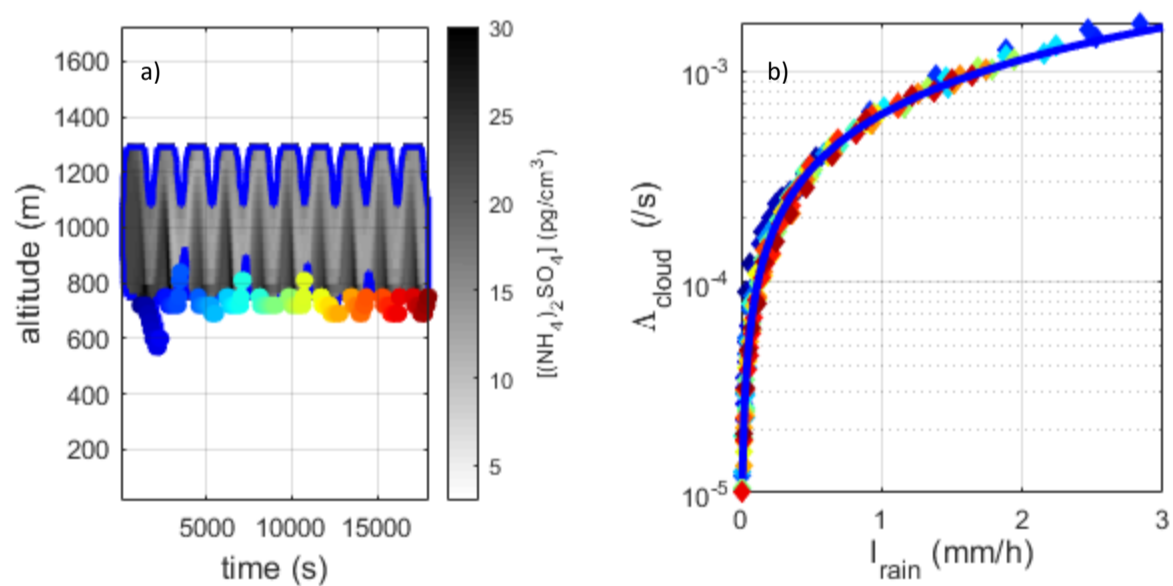
Figure 17. On the left: spatial-temporal distribution of the ammonium sulfate concentration in the contour of the cloud (criterion based on the concentration of hydrometeors with a threshold set at 0.01 particle.cm$^3$). On the right: correlation between the scavenging coefficient and the precipitation intensity determined at the base of the cloud, (—) adjusted by a power law.

400

401 In these three figures, we observe that the contour introduced by Hiron (2017) for cumulonimbus (based on a separation between cloud water and
402 precipitation water, on the basis of a criterion on the size of hydrometeors, cf. section 1.2) is no longer applicable for the stratus, and gives highly dispersed
403 scavenging coefficient results, particularly for low rain intensity ($I < 2\ mm.h^{-1}$). This is because, for this stratus, it is difficult to establish a strict boundary

between a raindrop and a cloud droplet, based on their size. However, the other two criteria yield bijective and similar relationships, both in terms of the cloud contours (Figure 15.a and Figure 17.a) and the adjusted power laws (Table 2). Unlike cumulonimbus, stratus contours appear to be reliable using a criterion based on relative humidity. This difference is related to the intensities of vertical flows in the cumulonimbus. Indeed, we observe in Figure 5 that, in the simulated cumulonimbus, the downdraft flows can be very intense (up to 5 m.s$^{-1}$), transporting to the base of the cloud air masses with a lower mixing ratio and hence lower relative humidity.

Table 2. Adjustment of scavenging coefficients by power laws for the three types of contours studied.

| Contour type | Power law adjustments |
|---|---|
| **Based on relative humidity (Figure 15)** | $\Lambda^m_{cloud} = 7.03 \times 10^{-4} I^{0.94}$ |
| **Based on mass concentration of cloud hydrometeors (Figure 16)** | $\Lambda^m_{cloud} = 2.10 \times 10^{-3} I^{1.16}$ |
| **Based on hydrometeor concentration (Figure 17)** | $\Lambda^m_{cloud} = 6.24 \times 10^{-4} I^{0.86}$ |

These calculations show that, regardless of the type of simulated cloud, cumulonimbus or stratus, the criterion based on the hydrometeor concentration makes it possible to yield cloud contours that are both stable (with little variation when the threshold value is varied), and for which the relationship between the scavenging coefficient and the rainfall intensity is the most biunivocal (Figure 8, Figure 9 and Figure 10 for cumulonimbus and Figure 15, Figure 16 and Figure 17 for stratus). This criterion is not directly accessible in meteorological models; however, examination of Figure 10 and Figure 17 suggests that the cloud base remains stable over time. It would therefore be possible to assess the altitude at which critical supersaturation is reached, and to consider this altitude constant over a period that depends on the ratio between the size of the grid cell and the velocity of the horizontal flows.

### 2.3. Comparison with the literature and unification of the scavenging coefficient scheme for a cumulonimbus and a stratus

There is insufficient data to compare our theoretical findings with field study data. Few experimental data have established *in situ* scavenging coefficients for different types of clouds. Based on caesium-137 deposition measured following the Fukushima Daiichi accident, Leadbetter *et al.*, (2015) used the Met Office dispersion model: NAME (Numerical Atmospheric-dispersion Modelling Environment) for the dispersion of the radioactive plume emitted during the accident, considering the meteorological data from the ECMWF model. The authors managed to determine the cloud scavenging coefficient which best suits the ground measurements of deposition (Kinoshita *et al.,* 2011). In the same general approach, but using the IRSN LdX dispersion model (Quélo *et al.*, 2007 and Groëll *et al.*, 2014) and meteorological data from MRI (Sekiyama *et al.*, 2017), Quérel *et al.* (2021) established a very similar scavenging coefficient. These two schemes are compared in Figure 18. The comparison is made using the $\kappa$ value of ammonium sulfate. This decision is based on the findings of the Kaneyasu et al. (2012) study, which demonstrated the long-distance transport of cesium-137 by these particles - a distance particularly relevant for in-cloud scavenging.
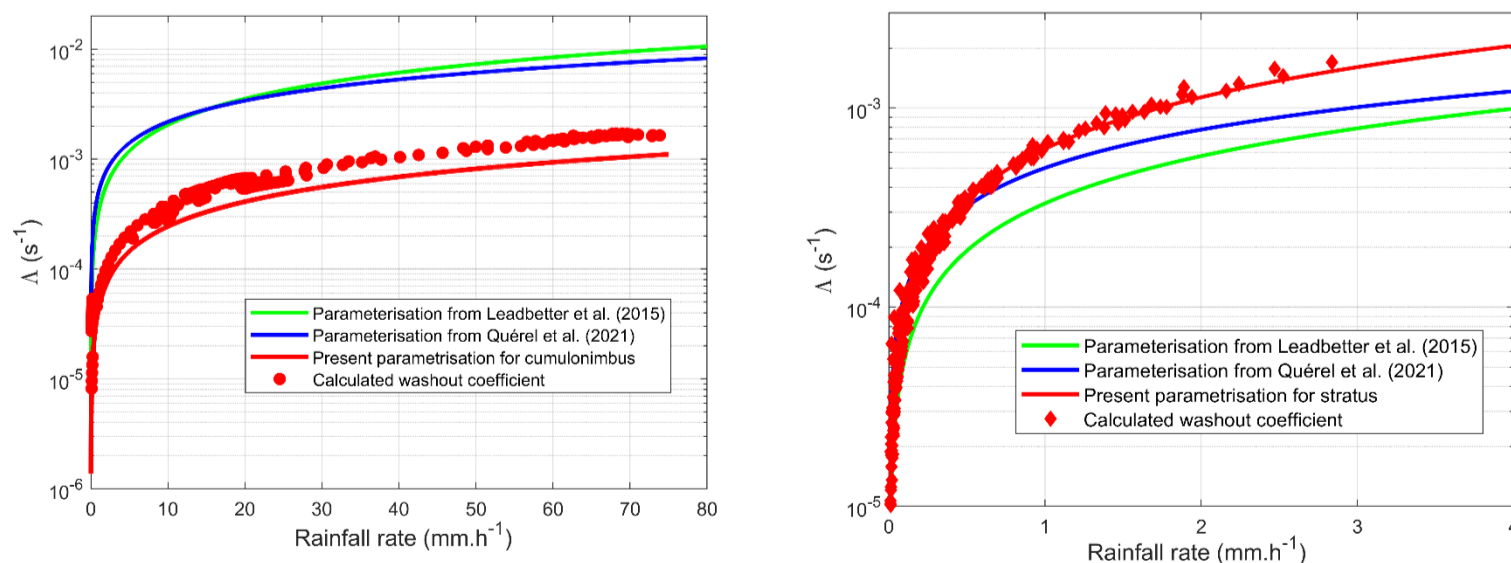
Figure 18. Comparison of the parameterisations established respectively for a cumulonimbus (left) and a stratus (right) with the parameterisations established by Leadbetter *et al.*, 2015 and Quérel *et al.*, 2021 following the Fukushima accident.

433    In this figure, we observe that the application of our scheme to a stratus (Figure 18, on the right), concords excellently with the parametrisation of scavenging

434    by clouds established following the Fukushima accident; in particular the parametrisation of Quérel *et al.*, (2021). However, the application of our approach

435    to cumulonimbus presents much greater differences. Indeed, over the entire rainfall intensity range, our results are on average six times lower than the

436    correlations of Leadbetter *et al.*, (2015) and Quérel *et al.*, (2021). Two questions therefore arise:

437    First, was there scavenging by cumulonimbus during the Fukushima accident? This would explain why it is difficult to compare our parametrisation of

438    scavenging by cumulonimbus with those deduced during the Fukushima accident.

439    Next, why, for the same rainfall intensity, do our calculations show that cumulonimbus scavenges less than stratus?

440    We will therefore address these two questions.

441    **Was there scavenging by cumulonimbus during the Fukushima accident?**

442    To answer this question, let us consider the distribution of rainfall intensities diagnosed from radar measurements by Saito *et al.*, (2015) during March 2011

443    in the Fukushima region (Figure 19). These results show that 80% of rain episodes diagnosed corresponded to rainfall intensities of less than 1.5 mm.h$^{-1}$,

444    and 97% to intensities of less than 3.5 mm.h$^{-1}$ (range of rainfall intensity produced at the base of the simulated stratus, Figure 15) and less than 0.01% had

445    intensities of more than 10 mm.h$^{-1}$. In view of these results, it is not possible to completely exclude the presence of rain issuing from cumulonimbus over

446    the period of the accident; however, if there was any, its contribution to the construction of the parameterisation of Leadbetter *et al.* (2015) and Quérel *et*

447    *al.* (2021) is negligible.
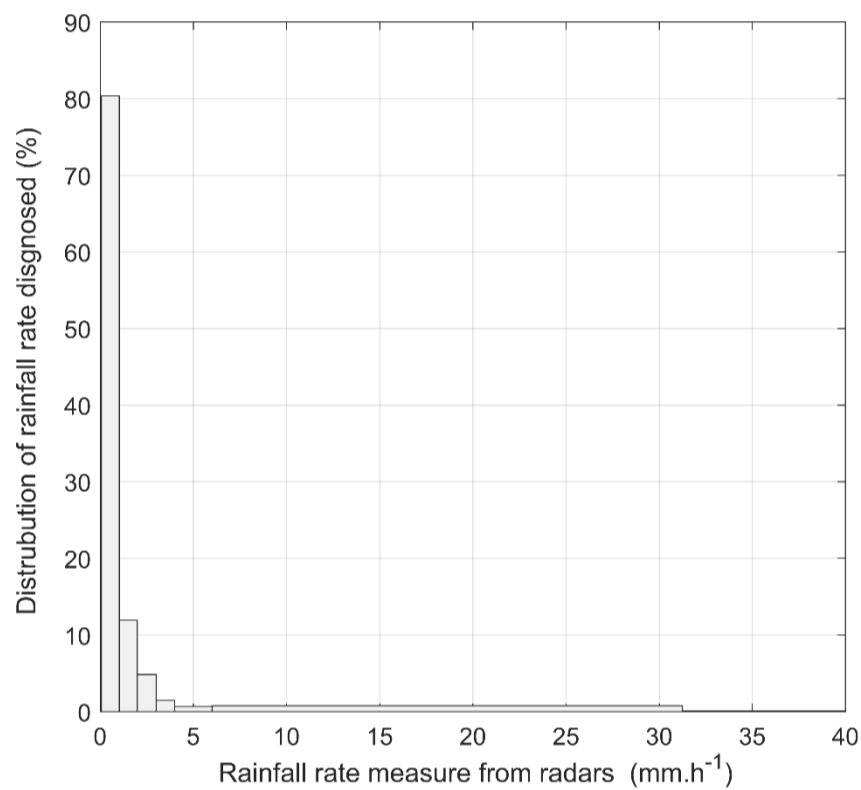
448

449            Figure 19. Distribution of rainfall intensity measured in the Fukushima region during March 2011 (Sekiyama *et al.*, 2017).

450

451    **How to unify the scavenging coefficient scheme for a cumulonimbus and a stratus?**

452    Our calculations show that cumulonimbus scavenges less than stratus under the same rainfall intensity. How can we understand this and unify the two

453    equations? This phenomenon can be attributed to the significantly higher level of supersaturation observed in cumulonimbus clouds (Figure 7.a) compared

454    to that in stratus cloud (Figure 13.a). Hence, if the supersaturation is higher, as is the case for cumulonimbus, for the same activated aerosol mass, these

455    particles are diluted in a larger mass of water, as the condensation is also much greater (in reality, the activated aerosol mass increases significantly since,

456    as we have indicated previously, the activation diameter of the aerosols decreases as supersaturation increases). Let us therefore examine the impact of

457    this effect of vapour condensation on the deduced parameterisation. In the DESCAM model, condensation is modelled by Equation 18. This equation is taken

458    from Pruppacher *et al.* (1998, chapter 13, section 2). It results from the vapour diffusion equation on a droplet of diameter $\mathcal{D}_{drop}$ in the air with

459    supersaturation $\mathcal{S}$ and temperature $T_\infty$, considering the thermodynamic equilibrium of the suspended drop within air using the $\kappa$-Köhler theory.

$$\begin{cases} \dfrac{d\mathcal{D}_{drop}}{dt} = \dfrac{4}{\mathcal{D}_{drop}} \dfrac{\mathcal{S}-y}{\dfrac{\rho_w \mathcal{R} T_\infty}{p_{sat,w} \mathfrak{D}_v M_w} + \dfrac{\mathcal{O}n\rho_w}{kT_\infty}\left(\dfrac{\mathcal{O}n\rho_w}{\mathcal{R}T_\infty}-1\right)} \\[20pt] y = \dfrac{4\,\sigma_{w,\mathcal{D}_{drop}} M_w}{\rho_w \mathcal{R} T_\infty \mathcal{D}_{drop}} - \kappa \dfrac{d_{ap}^{dry\,3}}{\mathcal{D}_{drop}^{\,3}} \end{cases} \qquad \text{Equation 18}$$

460

In this equation $\mathcal{R}$ is the ideal gas constant, $p_{sat,w}$ the saturating vapour pressure, $d_{ap}^{dry}$ the dry diameter of the aerosol, $\mathcal{On}$ the latent heat of vaporisation of the water, $\sigma_{w,\mathcal{D}_{drop}}$ the surface tension, $k$ the thermal conductivity of the air, $M_w$ and $\rho_w$ the molar mass and density of the water vapour, and finally $\mathfrak{D}_v$ the diffusion coefficient of the water vapour in air. As the Kelvin effect (linked to the curvature of the interface) and the solute effect become very quickly negligible after activation of the aerosol, this equation can be greatly simplified and reduced to: $\mathcal{D}_{drop}d\mathcal{D}_{drop} = \mathbb{C}.\mathcal{S}dt$, where $\mathbb{C}$ is a constant, enabling it to be integrated analytically, to give: $\mathcal{D}_{drop}(t) = \sqrt{\mathcal{D}_{drop,t_0}{}^2 + 2\mathbb{C}.\mathcal{S} \cdot t}$. Thus, to assess the effect of dilution of the aerosol in the droplet due to condensation, we can write:

$$\frac{\mathcal{D}_{drop}(t)^2_{stratus}}{\mathcal{D}_{drop}(t)^2_{cumulonimbus}} = \frac{\mathcal{D}_{drop,t_0}{}^2 + 2\mathbb{C}.\langle\mathcal{S}\rangle_{stratus} \cdot t_{stratus}}{\mathcal{D}_{drop,t_0}{}^2 + 2\mathbb{C}.\langle\mathcal{S}\rangle_{cumulonimbus} \cdot t_{cumulonimbus}} \qquad \text{Equation 19}$$

Attention: In this equation, $\mathcal{D}_{drop}(t)_{stratus}$ and $\mathcal{D}_{drop}(t)_{cumulonimbus}$ are not the diameters of the droplets in the stratus and in the cumulonimbus, but the diameters they would have had, if only the condensation mechanism had caused them to grow. We are in fact seeking to assess how large will be the dilution of aerosol material in the droplets related to vapour condensation. There are other mechanisms modelled in DECAM (such as coalescence or riming, Figure 2) that lead to the growth of hydrometeors, without necessarily diluting the aerosols in the droplets. If there had only been the condensation mechanism, we could have used Figure 14 directly to assess this dilution.

For long periods of time, further simplification can still be made because $\mathcal{D}_{drop,t_0}{}^2 \ll \mathcal{D}_{drop}(t)^2_{stratus} < \mathcal{D}_{drop}(t)^2_{cumulonimbus}$. Finally, we can write:

$$\frac{\mathcal{D}_{drop}(t)^2_{stratus}}{\mathcal{D}_{drop}(t)^2_{cumulonimbus}} = \frac{.\langle\mathcal{S}\rangle_{stratus} \cdot t_{stratus}}{\langle\mathcal{S}\rangle_{cumulonimbus} \cdot t_{cumulonimbus}} \qquad \text{Equation 20}$$

In this equation, the times $t_{stratus}$ and $t_{cumulonimbus}$ are therefore the times necessary for the formation of precipitation under the cloud. For each of the types of cloud, we observe in Figure 6.a and Figure 12.a that these times are very similar ($\approx$2200 s), which allows us to write:

$$\frac{\mathcal{D}_{drop}(t)_{stratus}}{\mathcal{D}_{drop}(t)_{cumulonimbus}} = \sqrt{\frac{\langle\mathcal{S}\rangle_{stratus}}{\langle\mathcal{S}\rangle_{cumulonimbus}}} \qquad \text{Equation 21}$$

The numerical application of this equation highlights a condensation growth ratio of a factor 2.3 between cumulonimbus and stratus. In mass, this coefficient corresponds to a dilution factor of 12. However, Figure 18 shows that, with this new approach, we can calculate that cumulonimbus scavenges 6 times less than stratus. This explanation is therefore satisfactory in view of all the hypotheses that have been made, especially since we have considered that the activated aerosol mass remained constant when supersaturation increased. We therefore propose a new generic parametrisation to any type of cloud, which this time considers this condensation-related dilution effect, Equation 22. This scavenging scheme is therefore corrected by a coefficient $1/\langle\mathcal{S}\rangle_{cloud}^{3/2}$ which characterises the dilution related to the growth of droplets by condensation:

$$\Lambda_{cloud}^m = \frac{5 \times 10^{-8}}{\langle\mathcal{S}\rangle_{cloud}^{3/2}} I^{0.75} \qquad \text{Equation 22}$$

The application of this new correlation, presented in Figure 20 shows an excellent match both for the cumulonimbus and for the simulated stratus. It remains to be considered whether supersaturation is accessible in the NWPs and, if so, if the horizontal resolutions of 1 to 10 km of such models are sufficiently representative of a real cloud.
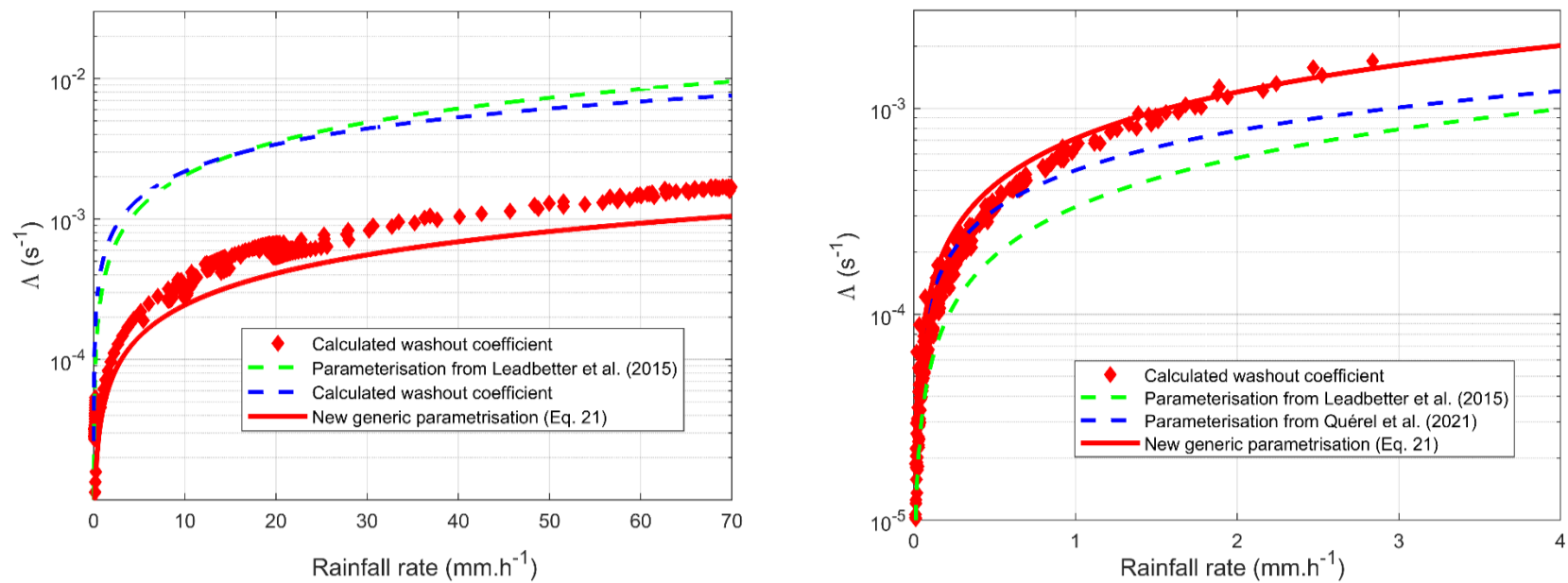
Figure 20. Comparison of the newly developed correlation Equation 22 with the scavenging modelled by DESCAM for a cumulonimbus and a stratus.

## 3. Conclusions

The in-cloud scavenging scheme established in this article shows a dependence on rain intensity and average supersaturation in the cloud. Supersaturation allows the scheme to be applicable to both cumulonimbus and stratus clouds. If supersaturation in the cloud is not accessible, it is still possible to apply a different scheme for convective clouds and stratiform clouds. But, since this boundary between the two types of cloud may be ambiguous, it will be preferable to apply the scheme with supersaturation if available.

This scavenging scheme is based on the DESCAM microphysical cloud model. This model allows fine-scale description of the life cycle of a cloud up to precipitation development. It tracks particles, crystals, and droplets particle size distributions and models all the water phase changes and, above all, how aerosol particles impact them. The in-cloud scavenging scheme is established by calculating the mass fluxes of particle material exiting the cloud being included in precipitation hydrometeors (both liquid and solid) and based on the mass of particles initially present in the cloud volume.

This calculation of cloud volume has proved to be a complex issue, in particular for establishing the altitude of the cloud base, especially when rain occurs. The most relevant method to identify cloud base in this study has been proven to be the one using the number of hydrometeors, rather than the relative humidity or the mass of the hydrometeors. The problem with this method is that this information on the number is not available for most of the NWPs. The use of the in-cloud scavenging scheme must be based on a diagnostic independent of the altitude of the base – and the summit – of the cloud.

In the case of stratus cloud, the parametrisation obtained with DESCAM is close to those currently used in the NAME and LdX atmospheric dispersion models, which were established on the basis of the Fukushima accident. As the precipitation that caused deposition of radioactive particles following the accident was largely generated by stratiform clouds, this study confirms *a posteriori* the choice of the in-cloud deposition scheme used to study radioactive deposition following the Fukushima accident and can be extended to all types of cloud.

In future works, this deposition scheme will be used with confidence to study deposition. As an example, it can be used for the deposition of radon progeny (Quérel *et al.,* 2022), in order to statistically measure the impact of this scheme in relation to the existing corpus.

Beyond the applications and validations of the scheme described in this article, the scheme itself is currently being refined. First of all, we are working on establishing an in-cloud scavenging rate that will depend on particle size. This important issue was discussed in section 1.3, and requires some modifications to the model to establish a model spectrally. This will make it possible to apply a finer-scale scheme to the atmospheric models with a spectral representation of the particles.

The influence of the coefficient $\kappa$ of the $\kappa$-Köhler theory can be also examined. This will make it possible to measure the importance of the physical-chemical properties of the particles: what error is made by applying the same scavenging rate for a hygroscopic aerosol (salt or sulfate) and a non-hygroscopic aerosol (soot, desert dust).

The initial particle size distribution of aerosols could also have a significant influence on the final scavenging rate. A distribution centred on 100 nm will not create the same cloud as the same total mass centred around 5 μm particles. This aspect must be assessed.

520     The question of evaporation of droplets between the cloud base and the ground has not yet been addressed. The scheme developed is based on the
521     precipitation intensity at the cloud base, but in the models the precipitation intensity is diagnosed on the ground. This is important for the applicability of
522     the scheme and this difference can lead to errors, especially in the event of high droplet evaporation.

523     Finally, it is not yet established that this scheme is as effective when applied to a model whose spatial resolution is lower than that of DESCAM, as is the
524     case for all Climate (GCM) and Transport (ATM) models.

525     The work still to be carried out will make it possible to best define the scope of validity of this new scheme for in-cloud aerosol scavenging, as well as the
526     uncertainties associated with this model. This will enable the scheme to be used in full knowledge of the facts and according to the highest scientific
527     standards.

528

529

## 530     **Competing interests**

531     The contact author has declared that none of the authors has any competing interests.

532

## References

534 Adachi K, Kajino M, Zaizen Y, Igarashi Y. Emission of spherical cesium-bearing particles from an early stage of the Fukushima nuclear accident. Sci Rep.
535 2013;3:2554. doi: 10.1038/srep02554. PMID: 23989894; PMCID: PMC3757362.

536 Asai, T., & Kasahara, A. (1967). A theoretical study of the compensating downward motions associated with cumulus clouds. *Journal of Atmospheric*
537 *Sciences*, *24*(5), 487-496.

538 American Meterological Society, 2020b: Glossary of meteorology: cloud. Website, accessed on October 21, 2020, URL http://
539 glossary.ametsoc.org/wiki/cloud.

540 Baklanov, A., & Sørensen, J. H. (2001). Parameterisation of radionuclide deposition in atmospheric long-range transport modelling. Physics and Chemistry
541 of the Earth, Part B: Hydrology, Oceans and Atmosphere, 26(10), 787-799.

542 Bigg, E. K. (1953). The formation of atmospheric ice crystals by the freezing of droplets. *Quarterly Journal of the Royal Meteorological Society*, *79*(342), 510-
543 519.

544 Beard, K. V. (1974). Experimental and numerical collision efficiencies for submicron particles scavenged by small raindrops. *Journal of Atmospheric*
545 *Sciences*, *31*(6), 1595-1603.

546 Bergeron, T. (1928). *Über die dreidimensional verknüpfende Wetteranalyse. 1. Prinzipielle Einführung in das Problem der Luftmassen-und Frontenbildung.*
547 na. Bony, S., & Dufresne, J. L. (2005). Marine boundary layer clouds at the heart of tropical cloud feedback uncertainties in climate models. *Geophysical*
548 *Research Letters*, *32*(20).

549 Clark, M. J., & Smith, F. B. (1988). Wet and dry deposition of Chernobyl releases. *Nature*, *332*(6161), 245-249.

550 Costa, M. J., Salgado, R., Santos, D., Levizzani, V., Bortoli, D., Silva, A. M., & Pinto, P. (2010). Modelling of orographic precipitation over Iberia: a springtime
551 case study. *Advances in Geosciences*, *25*, 103-110.

552 Croft, B., Lohmann, U., Martin, R. V., Stier, P., Wurzler, S., Feichter, J., ... & Ferrachat, S. (2010). Influences of in-cloud aerosol scavenging parameterizations
553 on aerosol concentrations and wet deposition in ECHAM5-HAM. *Atmospheric Chemistry and Physics*, *10*(4), 1511-1543.

554 De Cort, M. (1998). Atlas of caesium deposition on Europe after the Chernobyl accident.

555 Dépée, A., Lemaitre, P., Gelain, T., Mathieu, A., Monier, M., & Flossmann, A. (2019). Theoretical study of aerosol particle electroscavenging by clouds. *Journal*
556 *of Aerosol Science*, *135*, 1-20.

557 Dépée, A. (2019). *Etude expérimentale et théorique des mécanismes microphysiques mis en jeu dans la capture des aérosols radioactifs par les*
558 *nuages* (Doctoral dissertation, Université Clermont Auvergne [2017-2020]).

559 Dépée, A., Lemaitre, P., Gelain, T., Monier, M., & Flossmann, A. (2021). Laboratory study of the collection efficiency of submicron aerosol particles by cloud
560 droplets–Part I: Influence of relative humidity. *Atmospheric Chemistry and Physics*, *21*(9), 6945-6962.

561 Dépée, A., Lemaitre, P., Gelain, T., Monier, M., & Flossmann, A. (2021). Laboratory study of the collection efficiency of submicron aerosol particles by cloud
562 droplets–Part II: Influence of electric charges. *Atmospheric Chemistry and Physics*, *21*(9), 6963-6984.

563 Dye, J. E., Jones, J. J., Winn, W. P., Cerni, T. A., Gardiner, B., Lamb, D., ... & Saunders, C. P. R. (1986). Early electrification and precipitation development in a
564 small, isolated Montana cumulonimbus. *Journal of Geophysical Research: Atmospheres*, *91*(D1), 1231-1247.

565 Ervens, B. (2015). Modeling the processing of aerosol and trace gases in clouds and fogs. *Chemical reviews*, *115*(10), 4157-4198.

566 Findeisen, Z. (1938). Kolloid meteorologische vorgange bei neiderschlags-bildung. *Meteorologische Zeitschrift*, *55*, 121.

567 Flossmann, A. I., Hall, W. D., & Pruppacher, H. R. (1985). A theoretical study of the wet removal of atmospheric pollutants. Part I: The redistribution of aerosol
568 particles captured through nucleation and impaction scavenging by growing cloud drops. *Journal of Atmospheric Sciences*, *42*(6), 583-606.

569 Flossmann, A. I., Pruppacher, H. R., & Topalian, J. H. (1987). A theoretical study of the wet removal of atmospheric pollutants. Part II: The uptake and
570 redistribution of (NH 4) 2 SO 4 particles and SO 2 gas simultaneously scavenged by growing cloud drops. *Journal of Atmospheric Sciences*, *44*(20), 2912-2923.

571 Flossmann, A. I., & Pruppacher, H. R. (1988). A theoretical study of the wet removal of atmospheric pollutants. Part III: The uptake, redistribution, and
572 deposition of (NH 4) 2 SO 4 particles by a convective cloud using a two-dimensional cloud dynamics model. *Journal of Atmospheric Sciences*, *45*(13), 1857-
573 1871.

574 Flossmann, A. I. (1998). Clouds and pollution. *Pure and applied chemistry*, *70*(7), 1345-1352.

Flossmann, A. I., & Wobrock, W. (2010). A review of our understanding of the aerosol–cloud interaction from the perspective of a bin resolved cloud scale modelling. *Atmospheric Research*, *97*(4), 478-497.

Groëll, J., Quélo, D., & Mathieu, A. (2014). Sensitivity analysis of the modelled deposition of 137 Cs on the Japanese land following the Fukushima accident. International Journal of Environment and Pollution, 55(1-4), 67-75.

Hertel, O., Christensen, J., Runge, E. H., Asman, W. A., Berkowicz, R., Hovmand, M. F., & Hov, Ø. (1995). Development and testing of a new variable scale air pollution model—ACDEP. *Atmospheric Environment*, *29*(11), 1267-1290.

Hirsch, E., Koren, I., Levin, Z., Altaratz, O., & Agassi, E. (2014). On transition-zone water clouds. *Atmospheric Chemistry and Physics*, *14*(17), 9001-9012.

Hiron, T., & Flossmann, A. I. (2015). A study of the role of the parameterization of heterogeneous ice nucleation for the modeling of microphysics and precipitation of a convective cloud. *Journal of the Atmospheric Sciences*, *72*(9), 3322-3339.

Hiron, T. (2017). *Experimental and modeling study of heterogeneous ice nucleation on mineral aerosol particles and its impact on a convective cloud* (Doctoral dissertation, Université Clermont Auvergne).

Kaneyasu, N., Ohashi, H., Suzuki, F., Okuda, T., & Ikemori, F. (2012). Sulfate aerosol as a potential transport medium of radiocesium from the Fukushima nuclear accident. *Environmental science & technology*, *46*(11), 5720-5726.

Kerker, M., & Hampl, V. (1974). Scavenging of Aerosol Particles by a Failing Water Drop and Calculation of Washout Coefficients. *Journal of Atmospheric Sciences*, *31*(5), 1368-1376.

Kinoshita, N., Sueki, K., Sasa, K., Kitagawa, J. I., Ikarashi, S., Nishimura, T., ... & Yamagata, T. (2011). Assessment of individual radionuclide distributions from the Fukushima nuclear accident covering central-east Japan. *Proceedings of the National Academy of Sciences*, *108*(49), 19526-19529.

Knight, C. A. (1982). The cooperative convective precipitation experiment (CCOPE), 18 May–7 August 1981. *Bulletin of the American Meteorological Society*, *63*(4), 386-398.

Koop, T., Luo, B., Tsias, A., & Peter, T. (2000). Water activity as the determinant for homogeneous ice nucleation in aqueous solutions. *Nature*, *406*(6796), 611-614.

Laguionie, P., Roupsard, P., Maro, D., Solier, L., Rozet, M., Hébert, D., & Connan, O. (2014). Simultaneous quantification of the contributions of dry, washout and rainout deposition to the total deposition of particle-bound 7Be and 210Pb on an urban catchment area on a monthly scale. Journal of aerosol science, 77, 67-84.

Lai, K. Y., Dayan, N., & Kerker, M. (1978). Scavenging of aerosol particles by a falling water drop. *Journal of Atmospheric Sciences*, *35*(4), 674-682.

Leadbetter, S. J., Hort, M. C., Jones, A. R., Webster, H. N., & Draxler, R. R. (2015). Sensitivity of the modelled deposition of Caesium-137 from the Fukushima Dai-ichi nuclear power plant to the wet deposition parameterisation in NAME. *Journal of environmental radioactivity*, *139*, 200-211.

Leaitch, W., Strapp, J. W., Isaac, G. A., & Hudson, J. G. (1986). Cloud droplet nucleation and cloud scavenging of aerosol sulphate in polluted atmospheres. *Tellus B: Chemical and Physical Meteorology*, *38*(5), 328-344.

Lemaitre, P., Quérel, A., Monier, M., Menard, T., Porcheron, E., & Flossmann, A. I. (2017). Experimental evidence of the rear capture of aerosol particles by raindrops. *Atmospheric Chemistry and Physics*, *17*(6), 4159-4176.

Leroy, D., Monier, M., Wobrock, W., & Flossmann, A. I. (2006). A numerical study of the effects of the aerosol particle spectrum on the development of the ice phase and precipitation formation. *Atmospheric Research*, *80*(1), 15-45.

Leroy, D., Wobrock, W., & Flossmann, A. I. (2007). On the influence of the treatment of aerosol particles in different bin microphysical models: a comparison between two different schemes. *Atmospheric research*, *85*(3-4), 269-287.

Meyers, M. P., DeMott, P. J., & Cotton, W. R. (1992). New primary ice-nucleation parameterizations in an explicit cloud model. *Journal of Applied Meteorology and Climatology*, *31*(7), 708-721.

Monier, M., Wobrock, W., Gayet, J.-F., Flossmann, A., (2006). Development of a detailed microphysics cirrus model for interpretation of the recent INCA campaign. J. Amtos. Sci. 163.

Mathieu, A., Korsakissok, I., Quélo, D., Groëll, J., Tombette, M., Didier, D., ... & Isnard, O. (2012). Atmospheric dispersion and deposition of radionuclides from the Fukushima Daiichi nuclear power plant accident. Elements, 8(3), 195-200.

MRI, 2015. JMA-RATM Technical Report, vol. 76.

Palmer, T. (2014). Climate forecasting: Build high-resolution global climate models. *Nature*, *515*(7527), 338-339.

618 Petters, M. D., & Kreidenweis, S. M. (2007). A single parameter representation of hygroscopic growth and cloud condensation nucleus activity. *Atmospheric*

619 *Chemistry and Physics*, *7*(8), 1961-1971.

620 Petroff, A., Mailliat, A., Amielh, M., & Anselmet, F. (2008). Aerosol dry deposition on vegetative canopies. Part I: review of present knowledge. *Atmospheric*

621 *Environment*, *42*(16), 3625-3653.

622 Pranesha, T. S., & Kamra, A. K. (1996). Scavenging of aerosol particles by large water drops: 1. Neutral case. *Journal of Geophysical Research:*

623 *Atmospheres*, *101*(D18), 23373-23380.

624 Pruppacher, H. R., Klett, J. D., & Wang, P. K. (1998). Microphysics of clouds and precipitation. 2nd ed., Atmospheric and Oceanographic Sciences Library,

625 Kluwer Academic Publishers, doi:10.1080/02786829808965531.

626 Quélo, D., Krysta, M., Bocquet, M., Isnard, O., Minier, Y., & Sportisse, B. (2007). Validation of the Polyphemus platform on the ETEX, Chernobyl and Algeciras

627 cases. *Atmospheric environment*, *41*(26), 5300-5315.

628 Quérel, A., Monier, M., Flossmann, A. I., Lemaitre, P., & Porcheron, E. (2014). The importance of new collection efficiency values including the effect of rear

629 capture for the below-cloud scavenging of aerosol particles. *Atmospheric research*, *142*, 57-66.

630 Quérel, A., Quelo, D., Roustan, Y., & Mathieu, A. (2021). Sensitivity study to select the wet deposition scheme in an operational atmospheric transport

631 model. *Journal of Environmental Radioactivity*, *237*, 106712.

632 Quérel, A., Meddouni, K., Quélo, D., Doursout, T., Chuzel, S., 2022. Statistical approach to assess radon-222 long-range atmospheric transport modelling and

633 its associated gamma dose rate peaks, in: Advances in Geosciences. Presented at the Geoscience applications of environmental radioactivity - EGU General

634 Assembly 2021, Online, 19–30 April 2021, Copernicus GmbH, pp. 109–124.

635 Saito, K., Shimbori, T., & Draxler, R. (2015). JMA's regional atmospheric transport model calculations for the WMO technical task team on meteorological

636 analyses for Fukushima Daiichi Nuclear Power Plant accident. *Journal of environmental radioactivity*, *139*, 185-199.

637 Sassen, K., and B. S. Cho, 1992: Subvisual-thin cirrus lidar dataset for satellite verification and climatological research. J. Appl. Meteorol., 31, 1275–1285,

638 doi:10.1175/1520-0450(1992) 031<1275:STCLDF>2.0.CO;2, https://doi.org/10.1175/1520-0450(1992)031<1275:STCLDF>

639 2.0.CO;2.

640 Saito, K., Shimbori, T., & Draxler, R. (2015). JMA's regional atmospheric transport model calculations for the WMO technical task team on meteorological

641 analyses for Fukushima Daiichi Nuclear Power Plant accident. Journal of environmental radioactivity, 139, 185-199.

642 Sievering, H., Van Valin, C. C., Barrett, E. W., & Pueschel, R. F. (1984). Cloud scavenging of aerosol sulfur: Two case studies. *Atmospheric Environment*

643 *(1967)*, *18*(12), 2685-2690.

644 Slinn, W. G. N.: Some approximations for the wet and dry removal of particles and gases from the atmosphere, Water Air Soil Poll.,7, 513–543, 1977.

645 Spänkuch, D., Hellmuth, O., & Görsdorf, U. (2022). What is a cloud? Toward a more precise definition?. *Bulletin of the American Meteorological Society*.

646 Stephan, K., Klink, S., & Schraff, C. (2008). Assimilation of radar-derived rain rates into the convective-scale model COSMO-DE at DWD. *Quarterly Journal of*

647 *the Royal Meteorological Society: A journal of the atmospheric sciences, applied meteorology and physical oceanography*, *134*(634), 1315-1326.

648 Textor, C., Schulz, M., Guibert, S., Kinne, S., Balkanski, Y., Bauer, S., ... & Tie, X. (2006). Analysis and quantification of the diversities of aerosol life cycles

649 within AeroCom. *Atmospheric Chemistry and Physics*, *6*(7), 1777-1813.

650 Wegener, A. (1911). *Thermodynamik der atmosphäre*. JA Barth.

651 Vali, G., DeMott, P. J., Möhler, O., & Whale, T. F. (2015). A proposal for ice nucleation terminology. *Atmospheric Chemistry and Physics*, *15*(18), 10263-10270.

652 Vohl, O., Mitra, S. K., Wurzler, S. C., & Pruppacher, H. R. (1999). A wind tunnel study of the effects of turbulence on the growth of cloud drops by collision

653 and coalescence. *Journal of the atmospheric sciences*, *56*(24), 4088-4099.

654 Wang, H., & Su, W. (2013). Evaluating and understanding top of the atmosphere cloud radiative effects in Intergovernmental Panel on Climate Change (IPCC)

655 Fifth Assessment Report (AR5) Coupled Model Intercomparison Project Phase 5 (CMIP5) models using satellite observations. *Journal of Geophysical*

656 *Research: Atmospheres*, *118*(2), 683-699.

657 WMO. (2014). Guide to Meteorological Instruments and Methods of Observation (CIMO Guide, WMO-No. 8. Wood, R., & Field, P. R. (2011). The distribution

658 of cloud horizontal sizes. Journal of Climate, 24 (18), 4800-4816.

659 Zhang, L., Michelangeli, D. V., & Taylor, P. A. (2004). Numerical studies of aerosol scavenging by low-level, warm stratiform clouds and

660 precipitation. *Atmospheric Environment*, *38*(28), 4653-4665.

661    Zhang, S., Xiang, M., Xu, Z., Wang, L., & Zhang, C. (2020). Evaluation of water cycle health status based on a cloud model. *Journal of cleaner production*, *245*,

662    118850.